catalysts

MDPI

Article

Oxidative Steam Reforming of Methanol over Cu-Based Catalysts

Matteo Tommasi [1,†], Davide Ceriotti [1,2,†], Alice Gramegna [1,3], Simge Naz Degerli [3], Gianguido Ramis [4,5] and Ilenia Rossetti [1,3,6,*]

[1] Chemical Plants and Industrial Chemistry Group, Dipartimento di Chimica, Università Degli Studi di Milano, Via C. Golgi 19, 20133 Milan, Italy; matteo.tommasi@unimi.it (M.T.); davide.ceriotti@polimi.it (D.C.); alice.gramegna@unimi.it (A.G.)
[2] Dipartimento di Chimica, Materiali e Ingegneria Chimica, Politecnico di Milano, Via Mancinelli 7, 20131 Milan, Italy
[3] INSTM Unit Milano-Università, Via C. Golgi 19, 20133 Milan, Italy; simge.naz.degerli@guest.unimi.it
[4] Dipartimento di Ingegneria Chimica, Civile ed Ambientale, Università Degli Studi di Genova, Via all'Opera Pia 15A, 16145 Genoa, Italy; gianguidoramis@unige.it
[5] INSTM Unit Genova, Via all'Opera Pia 15A, 16145 Genoa, Italy
[6] Institute of Chemical Sciences and Technologies "Giulio Natta" (SCITEC), CNR, Via Golgi 19, 20133 Milano, Italy
* Correspondence: ilenia.rossetti@unimi.it; Tel.: +39-02-50314059
† These authors contributed equally to this work.

Abstract: Several Cu and Ni-based catalysts were synthetized over Ce-based supports, either pure or mixed with different amounts of alumina (1:2 and 1:3 mol/mol). Different metal loadings (10–40 wt%) and preparation methods (wet impregnation, co-precipitation, and flame-spray pyrolysis—FSP) were compared for the oxidative steam reforming of methanol. Characterization of the catalysts has been performed, e.g., through XRD, BET, XPS, TPR, SEM, and EDX analyses. All the catalysts have been tested in a bench-scale continuous setup. The hydrogen yield and methanol conversion obtained have been correlated with the operating conditions, metal content, crystallinity of the catalyst particles, total surface area, and with the interaction of the metal with the support. A Cu loading of 20% wt/wt was optimal, while the presence of alumina was not beneficial, decreasing catalyst activity at low temperatures compared with catalysts supported on pure CeO_2. Ni-based catalysts were a possible alternative, but the activity towards the methanation reaction at relatively high temperatures decreased inevitably the hydrogen yield. Durability and deactivation tests showed that the best-performing catalyst, 20% wt. Cu/CeO_2 prepared through coprecipitation was stable for a long period of time. Full methanol conversion was achieved at 280 °C, and the highest yield of H_2 was ca. 80% at 340 °C, higher than the literature data.

Keywords: oxidative steam reforming of methanol; methanol reforming; Cu-based catalysts; hydrogen production; CuO/CeO_2 catalysts; ceria

Citation: Tommasi, M.; Ceriotti, D.; Gramegna, A.; Degerli, S.N.; Ramis, G.; Rossetti, I. Oxidative Steam Reforming of Methanol over Cu-Based Catalysts. *Catalysts* **2024**, *14*, 759. https://doi.org/10.3390/catal14110759

Academic Editor: Binlin Dou

Received: 8 September 2024
Revised: 15 October 2024
Accepted: 22 October 2024
Published: 28 October 2024

1. Introduction

Currently, 55 million tons of H_2 are produced annually, with 95% of that amount coming from fossil fuels. About 50% of the hydrogen produced by steam reforming comes from natural gas, 30% from oil and naphtha, 18% from coal gasification, and 4% from water electrolysis [1,2].

As stated, most of the hydrogen production comes from methane reforming, in particular, the steam–methane reforming reaction coupled with the water–gas shift reaction. Although this pathway is effective, researchers are exploring new ways to produce hydrogen from renewable resources, such as bio-hydrocarbons, to produce "greener" hydrogen. Furthermore, to promote the use of green hydrogen for the energy transition, its storage and distribution issues are still unsolved. The conversion of H_2 into chemical hydrogen vectors

is becoming more and more popular since it can exploit conventional hydrogenation reactions, and the transportation of the produced chemicals (e.g., CH_4, NH_3, or CH_3OH) is very well established. Such vectors may be used as regenerated fuels by direct combustion [3], or split back to recover H_2, though this decomposition often introduces an energy penalty [4].

Biomass-derived methanol is also under development. Many projects and demonstrative plants are in progress for biomass-to-liquids (BtL) processing, which implies the conversion of biomass to syngas, e.g., by gasification [5] and the feed of the syngas to a methanol production unit. Biochemical processes are also on the way for the direct conversion of biomass into methanol, thanks to the fermentation process [6]. Furthermore, methanol production is currently studied from CO_2 streams [7], which implies the additional advantage of CO_2 utilization.

Methanol has various advantages for H_2 production than other liquid hydrocarbons. The reforming process can occur at low temperatures (200–350 °C), with respect to methane and higher homologs, thanks to the small amount of energy required to break the molecule, it has a high ratio of H_2/CO, it is a convenient for storage and transportation, and the risk of coke formation due to pyrolysis is lower for methanol than other hydrocarbons [8,9]. Furthermore, it is one of the rare compounds authorized by regulatory bodies for use in ship propulsion, unlike ethanol or hydrogen itself, which are, at the moment, not allowed in many countries. This would offer a hydrogen vector for use in fuel cells for sectors difficult to electrify, such as the maritime sector and air transport.

In addition to those applications that can directly exploit methanol as fuel or the case of emerging direct methanol fuel cells, it is interesting to consider the reversible release of hydrogen from methanol to feed conventional H_2 fuel cells, which are the ones commercially available at the moment, to demonstrate the feasibility of methanol as a green hydrogen vector.

There are mainly four reforming reactions (Equations (1)–(4)) for converting methanol into a hydrogen rich gas [10].

Steam reforming of methanol (SRM) is:

$$CH_3OH + H_2O \rightleftarrows CO_2 + 3H_2 \quad \Delta H^0 = 49.7\ kJ/mol \tag{1}$$

Partial oxidation of methanol (POM) is:

$$CH_3OH + 0.5O_2 \rightleftarrows CO_2 + 2H_2 \quad \Delta H^0 = -192.2\ kJ/mol \tag{2}$$

Methanol decomposition (MD) is:

$$CH_3OH \rightleftarrows CO + 2H_2 \quad \Delta H^0 = 128.5\ kJ/mol \tag{3}$$

Oxidative steam reforming of methanol (OSRM) is:

$$CH_3OH + 0.75\ H_2O + 0.125\ O_2 \rightleftarrows CO_2 + 2.75H_2\ \Delta H^0 = 0\ kJ/mol \tag{4}$$

While reactions (1) and (3) are endothermal, reaction (2) is exothermal, implying a difficult control of temperature and loss of selectivity. The process that is more advantageous from an energy efficiency standpoint is OSRM (4), which can function with an auto-thermal approach without the use of external heat. This, in principle, avoids external energy input in the cracking of the energy vector to recover H_2. Another benefit of OSRM is the ability to operate without the creation of carbon deposits at low temperatures between 150 and 330 °C. As a final remark, synthetic methanol has no sulfur, which is suitable for the reforming process with high activity, avoiding catalyst poisoning.

Despite several studies on the methanol-reforming and oxidative-reforming processes, the precise chemical mechanisms of OSRM remain widely unknown due to their complexity. The kinetics and routes of the reactions differ substantially depending on the catalysts utilized and the reaction conditions [11].

The literature reports many catalytic systems for this application [12–16]. In the present work, the attention is focused on Cu-based and Ni-based catalysts, which are supported over ceria and alumina in different molar ratios. The role of copper was deeply studied in the last decade for both SRM and OSRM, and according to the literature [17], Cu-based catalysts provide high CO_2 selectivity over undesired CO in the steam-reforming reaction. This is due to a chemical pathway in which adsorbed intermediate HCHO (formaldehyde) species combine with water to produce H_2 and CO_2 directly without the formation of a CO intermediate.

Cu/CeO_2 catalyst performance can be explained by the combination of copper states ($Cu^0/Cu^+/Cu^{2+}$) with widely dispersed Cu. Nonetheless, reaction intermediates cannot be ruled out and the precise mechanism is still unknown. The catalytic performance in OSRM appears to be significantly influenced by the strong interaction between the copper active species and the CeO_2 support [18].

The role of alumina in these catalysts is instead mainly physical. Alumina is known to have a large surface area and a high level of porosity. Furthermore, alumina is cheaper than ceria, and a mixture of the two compounds helps in reducing the cost of the final catalyst [19].

On the other hand, nickel-based catalysts have been largely investigated for the oxidative reforming of ethanol, due to the great ability of Ni to break C-C bonds and to enhance the water–gas shift processes. Ni demonstrated a very active and selective active phase for ethanol steam reforming [20], and this increases the hydrogen yield. For this reason, nickel catalysts were here prepared and tested to evaluate their performance in switching the reactant from ethanol to methanol. The main issues correlated with nickel-based catalysts could be the coke formation due to inefficient carbon gasification by steam [9], which could cause the deactivation of the catalyst, especially in the low-temperature regime applied during OSRM.

This work focuses on the design and optimization of catalysts for the conversion of methanol into hydrogen and carbon dioxide, with maximized selectivity to allow easy recovery and recycling in an efficient C-loop. Various Cu- and Ni-based catalysts, supported with different metal concentrations over ceria and alumina have been tested and characterized. The three main synthesis methodologies here employed were the co-precipitation method, the wet-impregnation method, and flame spray pyrolysis (FSP). Every catalyst studied has been characterized by XRD, BET, TPR, SEM, and EDX techniques, and the tests for OSRM have been carried out on a bench-scale continuous reactor, including durability tests for the most active sample.

2. Experimental

2.1. Catalysts Preparation

2.1.1. Precipitation Method

The precipitation or co-precipitation method is a simple but effective route to reach the final oxide. The first reaction between the metal precursor and the precipitating agent gives as a result the respective metal hydroxide, which is then oxidized and dehydrated through calcination [21]. Fundamental to reaching small and defined NiO and CuO nanoparticles is to optimize the precipitating system, from the nickel and copper precursor, the pH of the solution, the precipitating agent, and the calcination temperature and temperature gradient.

$Ce(NO_3)_3{\cdot}6H_2O$ (Sigma Aldrich, St. Louis, MO, USA, purity $\geq$ 99.0%), $Al(NO_3)_3{\cdot}9H_2O$ (Sigma Aldrich, purity $\geq$ 99.0%), and $Cu(NO_3)_3{\cdot}3H_2O$ (Sigma Aldrich, purity $\geq$ 99.5%) were used as precursors. A 1 M solution in water was prepared with different contents of copper (10 wt%, 20 wt%, and 40 wt%) and different molar ratios between ceria and alumina (1:0, 1:2, and 1:3 mol/mol).

After 1 h of stirring at 80 °C, an alkaline solution containing sodium carbonate 1 M (for the catalyst CU20%P-12 1°GEN) or sodium hydroxide 1 M (for all the other catalysts) was added dropwise until a pH of greater than 8 was reached. The solution was left to age at 70 °C for one hour and then 30 min at room temperature to cool down.

The precipitate was then filtered with a Buchner and washed with deionized water and pure ethanol. The filtered product was then dried overnight in an oven at 120 °C and subsequently calcined at 400 °C for 4 h in static air. This method was used to prepare also the ceria and ceria–alumina supports later used in the wet-impregnation (WI) synthesis.

2.1.2. Flame Spray Pyrolysis

Flame spray pyrolysis (FSP) is a synthesis technique for obtaining single or mixed oxides [22–25]. Usually, the metal oxide precursors are organic salts of the metal cation. These compounds are then dissolved in a flammable organic solvent and pumped with a syringe through a capillary tube at the center of a nozzle in the middle of the burner.

The capillary tube is coaxially lapped by an oxygen flow that serves as a comburent, while also dispersing the solution in very fine droplets. The heterogeneous mixture composed of oxygen and the precursor solution is ignited by twelve small flamelets, composed of a stoichiometric mixture of methane and oxygen, surrounding the nozzle. This creates the main flame with a temperature that depends on the solvent used and the precursors' nature and concentration [22,24–27]. In the flame, the instantaneous dispersion and vaporization of the precursor solution occur; the vapor undergoes a decomposition, in this case called pyrolysis; and some nanoparticles of metal oxide start to form. These nanoparticles then grow bigger in the nucleation process due to coalescence, sintering, and condensation. At the top of the flame, the nanoparticles reach the final dimension, which can be tuned depending on the flame temperature and the residence time in the hot zone. The dimensions of the particles depend on the residence time of the particles inside the flame; the temperature of the flame, which in turn depends on the solvent nature and concentration of precursors; and the density of the nanoparticles inside the solution [28].

The liquid is fed by a syringe pump (Harvard model 975, Holliston, MA, USA) that guarantees a constant flow of 2.7 mL/min of the precursor solution. The flows of oxygen and methane for the supporting flamelets were, respectively, 1000 mL/min and 500 mL/min. The central oxygen flow was sent through the nozzle, with a relative overpressure of 0.3 bar and with 5 L/min flow. With the FSP techniques, the following catalysts and supports were prepared:

- 10 wt% NiO supported on CeO_2;
- 20 wt% NiO supported on CeO_2.

$Ni(OCOCH_3)_2 \cdot 4H_2O$ (Sigma Aldrich, purity ≥98.0%) and $Ce(OCOCH_3)_3 \cdot H_2O$ (Sigma Aldrich, purity ≥ 99.9%) were used as precursors. The technique has been used for the preparation of Ni-based samples only based on previous experience with catalysts for the steam reforming of ethanol. The flame pyrolysis procedure requires a soluble precursor for the support and active phase, which should decompose rapidly in the flame in a solvent that does not evaporate instantaneously. Furthermore, the vapor pressure of Cu is much higher than that of Ni [29], leading to the difficult employment of this kind of preparation technique. As discussed in [23,27], the quality of the catalyst, in terms of dispersion of the active phase, stability, and interaction strength with the support, was much poorer in the case of FSP-prepared Cu-based catalysts rather than for Ni-based catalysts.

Some solubility tests have been performed to find a solution that could dissolve the precursors without losing the thermal enthalpy necessary for reaching a high temperature in the flame. Solubility tests were performed using acetic acid, propionic acid, and dimethylformamide (DMF) as solvents in different ratios. The use of propionic acid, although suggested by previous similar formulations, was discarded due to its poor ability to dissolve all the current precursors. Finally, a solution composed of 80% acetic acid and 20% DMF was selected with a concentration of 0.1 M.

2.1.3. Wet-Impregnation Method

The ceria or ceria–alumina supports were prepared through the two previously described methods, and subsequently, the active phase was added by impregnation using a rotavapor.

A solution 1 M of the catalyst support (ceria or ceria–alumina) was prepared and inserted in a flask; the temperature was set at 40 °C. Another 1 M solution prepared with the active phase precursor (Cu nitrate for precipitation and $Ni(NO_3)_2 \cdot 6H_2O$, Sigma Aldrich, purity ≥ 99.5%) was then added to the flask. After 2 h of stirring at 40 °C, the vacuum was activated to gently evaporate the solvent.

The obtained solid was washed with pure ethanol and filtered under vacuum, then dried overnight at 120 °C and calcined at 400 °C for 4 h in static air [30–32].

A summary of the samples prepared, and their corresponding codes, is reported in Table 1.

Table 1. Summary of samples prepared and their labeling.

Sample	Active Phase	Support (mol/mol)	Method
CU10%P-12	Cu (10 wt%)	CeO_2/Al_2O_3 (1:2)	Precipitation
CU20%P-12 1°G	Cu (20 wt%)	CeO_2/Al_2O_3 (1:2)	Precipitation
CU20%P-12	Cu (20 wt%)	CeO_2/Al_2O_3 (1:2)	Precipitation
CU20%P-13	Cu (20 wt%)	CeO_2/Al_2O_3 (1:3)	Precipitation
CU20%CERIA	Cu (20 wt%)	CeO_2	Precipitation
CU40%CERIA	Cu (40 wt%)	CeO_2	Precipitation
CU20%WI-12	Cu (20 wt%)	CeO_2/Al_2O_3 (1:2)	Wet impregnation
CU40%WI-12	Cu (40 wt%)	CeO_2/Al_2O_3 (1:2)	Wet impregnation
CU20%WI-13	Cu (20 wt%)	CeO_2/Al_2O_3 (1:3)	Wet impregnation
NI10%WI	Ni (10 wt%)	CeO_2	Wet impregnation
NI10%FSP	Ni (10 wt%)	CeO_2	Flame spray pyrolysis
NI20%FSP	Ni (20 wt%)	CeO_2	Flame spray pyrolysis

2.2. Catalysts Characterization

The characterization of the samples was carried out on the as-prepared materials, if not otherwise indicated.

XRD (X-ray diffraction) has been performed to evaluate the crystalline structure and phases present with a Rigaku Miniflex-600 horizontal scan powder diffractometer (Tokyo, Japan) using the Cu-Kα radiation with a graphite monochromator on the diffracted beam. The samples were analyzed at 2θ = 5–90°, with sampling every 0.016° and exposition every 27 s. The diffractograms were compared with the literature data reported in the JCPDS files [33]. The crystal sizes were calculated using the Scherrer Equation (5) [34]:

$$D = \frac{K\lambda}{\beta cos\theta} \quad (5)$$

where D is the crystallite size, K is a dimensionless shape factor with a typical value of 0.9, λ is the wavelength of the Cu-Kα X-ray= 1.5406 Å, θ is the Bragg angle, and β is the full width at half maximum (FWHM) evaluated for the most intense peak of the interesting phase. For copper oxide, β was evaluated at 2 θ = 38.60° (0 0 2), with the "FWHM" tool present in Origin software (version 2023b), while for nickel oxide, β was evaluated at 2 θ = 43.20° (corresponding to the 2 0 0 plane).

The N_2 adsorption and desorption isotherms were measured using a ASAP2020 instrument (Micromeritics, Norcross, GA, USA). The pore volume and BET SSA (Brunauer–Emmett–Teller specific surface area) were estimated using N_2 adsorption/desorption isotherms obtained at −196 °C for samples previously outgassed at 200 °C for 4 h. The BET linearization was performed to estimate the specific surface area in the range of 0.05–0.30p/p° (SSA_{BET}). The t-plot was applied to calculate micropores' volume. The Barrett–Joyner–Halenda (BJH) model was employed to determine the mesopore-size distribution from the desorption branch of the isotherm [35]. For each catalyst, its surface area, pore size, and relative distribution were evaluated with these techniques. The pores' shape, moreover, was determined thanks to the study of the hysteresis loop.

Scanning electron microscopy (SEM) pictures and energy dispersive X-ray analysis (EDX) spectra were obtained using a Hitachi^{TM} 1000 tabletop scanning electron microscope (Marunouchi, Chiyoda, Japan). SEM images have been taken at magnifications $\times$500, $\times$1500, and $\times$8000 to evaluate the shape and the dimension of the particle agglomerates. Thanks to the EDX and XPS analyses, furthermore, it was possible to assess the local composition of the catalyst surface.

X-ray photoelectron spectroscopy was carried out over an M-probe apparatus (Surface Science Instruments, Euroscan Instruments SA, Vedrin, Belgium). The source was monochromatic Al K radiation (1486.6 eV). A spot size of 200 · 750 µm and a pass energy of 25 eV were used. The hydrocarbon-contaminant C 1s level was taken as the internal reference at 284.6 eV. The position and full width at half-maximum (FWHM) of the C 1s line were carefully checked for every independent determination. The accuracy of the reported binding energies (BEs) can be estimated to be 0.1 eV. XPS high-resolution scans were acquired between 920 and 970 eV for Cu 2p.

Temperature-programmed reduction (TPR) analysis has been conducted with a CatLab microreactor system equipped with an online mass spectrometer gas analyzer (QGA) (Hyden Analytical, Warrington, UK). Tests have been performed with 35 mg of catalyst and a heating ramp of 10 °C/min up to 300 °C. A total flow of 50 mL/min was used during the analysis, composed of 10 mL/min of hydrogen diluted with 40 mL/min of He. Once 300 °C was reached, the sample was kept at this temperature for 1 h, with the same previous flow conditions. m/z = 2 (hydrogen) and 18 (water) were considered to follow the consumption of hydrogen due to the reduction and the formation of water as a product. After each analysis, a pulsed calibration with pure H_2 was performed. The consumption of hydrogen was evaluated through Gaussian peak profiling. The area obtained was converted to mmol H_2 consumed.

2.3. Activity Testing Procedure

The catalysts were pressed, crushed, and sieved, obtaining a particle size range between 0.15 and 0.25 mm. Mixed and loaded into the reactor were 0.5 g of SiC and 0.4 g of catalyst.

The experimental apparatus was mainly composed of a steel reactor and a cylindrical tube 40 cm long with an internal diameter of 0.9 cm. This reactor was then covered with a metal jacket to heat it in an oven, whose temperature was set and controlled by a Eurotherm 3204 TIC (Worthing, UK). Mass flow meters were used to inject a fixed amount of oxygen, nitrogen, and hydrogen, the latter only during the catalyst activation phase (Brooks Instrument. mod 0154, Brooks Mass Flow Controller mod. 5850 TR series, Hatfield, PA, USA). An HPLC pump (Waters, Milford, MA, USA, mod 501) was employed to inject the solution of methanol and water. Two IR heating lamps were added, one to evaporate the solution of methanol and water and one to avoid the possible condensation of the products outflowing the reactor. A collection flask was added at the reactor outlet, where the outgoing products are collected before being released in the vent for the possible collection of excess liquids if needed.

An Agilent (Santa Clara, CA, USA) 7890A gas chromatograph (GC) was used for the analysis of the gas. The GC was equipped with two columns: an Agilent HPPLOTQ, 25 m long, 0.53 mm internal diameter and a MoleSieve column, 15 m long, 0.53 mm internal diameter with molecular sieves as the stationary phase. A sampling loop of 250 µL was controlled by a rotary valve system, allowing for precise calibration methods without the use of an internal or external standard. The TCD detector allowed for quantification of the product's composition. Proper calibration was taken for CO_2, H_2, O_2, N_2, CH_4, CO, CH_3CHO, and CH_3OH.

Once the catalyst was loaded inside the reactor, a flow of nitrogen, 30 mL/min, was used for activation, and the temperature was set at 300 °C with a Eurotherm 3204 system. Once the temperature reached a mixture of 10 mL/min of hydrogen, 40 mL/min of nitrogen was sent to the reactor for 1.5 h. After the reduction, the system was cooled down to 200–250 °C, and a flow of pure nitrogen, 40 mL/min, was insufflated to remove the traces of hydrogen that were left. After 30 min, the test was started.

During the test, a mixture of 1.7 mL/min of oxygen and 40 mL/min of nitrogen was sent into the reactor, mixed with a flow of 0.025 mL/min of the mixture MeOH-H_2O (1:1 mol/mol) pre-vaporized. After two hours at the pre-fixed temperature, the outflowing gases were withdrawn with a syringe and analyzed with the GC. The tests were conducted in a range of temperatures between 200 °C and 390 °C. It must be considered that the indicated temperature was the nominal one, set by the regulator, while the actual temperature in the reactor core was ca. 20 °C less. After each temperature step, 1 h of equilibration was allowed before gas sampling.

A study on the deactivation was also carried out for the catalysts that showed better performance. At a fixed temperature of 280 °C, the reaction was carried out for 220 h on-stream.

To evaluate the performance, the hydrogen yield (Equation (6)), methanol conversion (Equation (7)), product distribution towards CO_2 and CO (Equations (8) and (9), respectively), and methane yield (Equation (10)) was calculated as follows:

$$\text{Hydrogen Yield} = \frac{\text{mol } H_2}{(\text{mol } CH_3OH)\text{input} \times 2.68} \quad (6)$$

$$\text{Methanol conversion} = \frac{\text{mol } CH_3OH \text{ input} - \text{mol } CH_3OH \text{ output}}{\text{mol } CH_3OH \text{ input}} \quad (7)$$

$$CO_2/CO_x \text{ ratio} = \frac{\text{mol } CO_2 \text{ out}}{\text{mol } CO_2 \text{ out} + \text{mol CO out}} \quad (8)$$

$$CO/CO_x \text{ ratio} = \frac{\text{mol CO out}}{\text{mol } CO_2 \text{ out} + \text{mol CO out}} \quad (9)$$

$$\text{Methane yield} = \frac{\text{mol } CH_4 \text{ out}}{\text{mol } CH_3OH \text{ input}} \quad (10)$$

3. Results

3.1. Catalysts Characterization

All the catalysts tested have been characterized. All of the XRD and SEM analyses are reported in the Supplementary Materials File, while the most significant results are implemented in the main text.

3.1.1. XRD

The reflections of CeO_2, CuO, NiO, and γ-Al_2O_3 were indexed according to JCPDS 75-0076, JCPDS 45-0937, JCPDS 47-1049, and JCPDS 29-0063 files, respectively [33]. Details about the pane indices and the structure type are reported in the Supplementary Materials. The XRD patterns of the three best-performing catalysts are here reported. Figure 1 shows the diffractograms of Cu20%P1-2, Cu20%WI1-2, and Cu20%-Ceria.

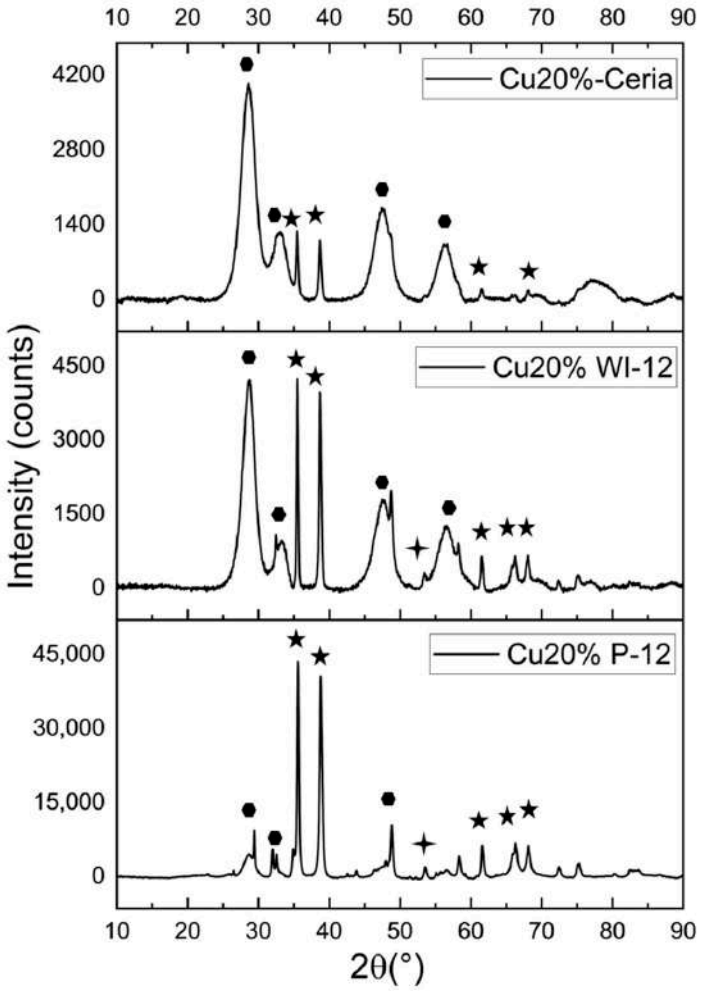

Figure 1. XRD analysis of Cu20% ceria, Cu20%WI-12, Cu20%P-12 (relevant phases: CuO ★ [JCPDS 45-0937], CeO_2 ● [JCPDS 75-0076], Al_2O_3 ✦ [JCPDS 29-0063]).

The XRD patterns of the catalysts synthetized clearly show the presence of the crystalline phase of CuO at 2θ equal to 35° and 38°, indexed by (0 0 2) and (1 1 1), respectively, (JCPDS 45-0937). The sharpness of the two peaks is an indication of the high crystallinity of the copper oxide present. Notably, the sample Cu20%P1-2 shows higher crystallinity of the CuO phase with respect to the support, which does not translate to a higher activity of the catalyst. The reflections attributable to CeO_2 (JCPDS 75-0076) were very broad due to lower crystallinity/smaller crystal size. CeO_2 features can be clearly observed at 2θ equal to 28.5°, 33°, 47.5°, and 56°, indexed by (1 1 1), (2 0 0), (2 2 0), and (3 1 1). The reflections ascribable to ceria were much more intense in the Cu20%-Ceria sample due to the higher concentration of CeO_2 present compared to the other two samples, which also contained Al_2O_3. The alumina reflections (JCPDS 29-0063) were not very evident with respect to the other two phases. Furthermore, the copper reflections were increasing in intensity with the increase of the copper loading, as expected.

The crystal size of the Cu-containing phase is reported in Table 2 and ranges between 26 and 30 nm for the samples supported over the alumina–ceria support. A similar crystal size was obtained for the samples prepared by coprecipitation and impregnation, while a much smaller size was achieved when supporting CuO_x over ceria (17–20 nm).

Table 2. Main physical–chemical properties of the prepared catalysts. * from EDX. ** from Scherrer equation. [a] This value became 18 nm after reduction. [b] This value became 16 nm after reduction.

Catalyst	SSA_{BET} (m^2/g)	Metal Loading (wt%) *	Crystal Size (nm) **
CU10%P-12	23	6.1	27
CU20%P-12 1°G	6.2	20.0	22
CU20%P-12	49	26.7	27
CU20%P-13	121	19.9	30
CU20%WI-12	95	16.4	28
CU40%WI-12	46	21.9	27
CU20%WI-13	75	12.8	26
CU20%CERIA	121	16.9	20 [a]
CU40%CERIA	44	23.7	17
NI10%FSP	9	9.5	17 [b]
NI20%FSP	16	19.3	18
NI10%WI	164	12.5	n.a.

In Figure 2, the XRD performed before and after reduction for both the Cu20% ceria and the Ni10% FSP ceria are reported. It can be noticed that, after the reduction, oxide reflections disappeared, and both the Cu (Figure 2a) and Ni reflections (Figure 2b) appeared. The Cu20% ceria sample showed signals at 2θ equal to 43°, 50°, and 74°, which are attributable to metallic Cu (JCPDS 03-1018) indexed by (1 1 1), (2 0 0), and (2 2 0), respectively. The Ni10% FSP ceria showed features at 2θ equal to 44° and 52°, which are attributable to metallic Ni (JCPDS 87-0712). The crystallite size calculated for the Cu and Ni reflections through the Scherrer equation showed similar results to the one calculated using the metal oxide, with values of 18 nm (Cu) and 16 nm (Ni) crystallites.

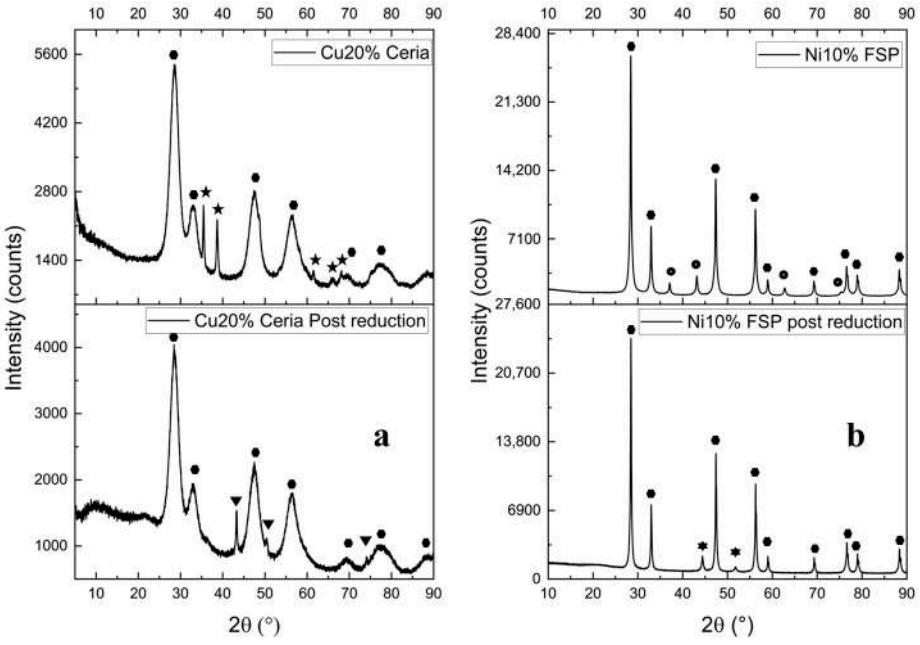

Figure 2. XRD analysis of Cu20% ceria (**a**) and Ni10% FSP ceria (**b**), pre- and post-reduction (relevant phases: CuO ★ [JCPDS 45-0937], Cu ▼ [JCPDS 03-1018], CeO_2 ⬢ [JCPDS 75-0076], NiO ⊙ [JCPDS 47-1049], and Ni ✸ [JCPDS 87-0712]).

3.1.2. SEM-EDX

Figure 3 presents the SEM images of the three best-performing catalysts at three different magnifications. The micrographs depict the shape of the agglomerates and their dimension in the small area analyzed. Other images can be found in the Supplementary Materials.

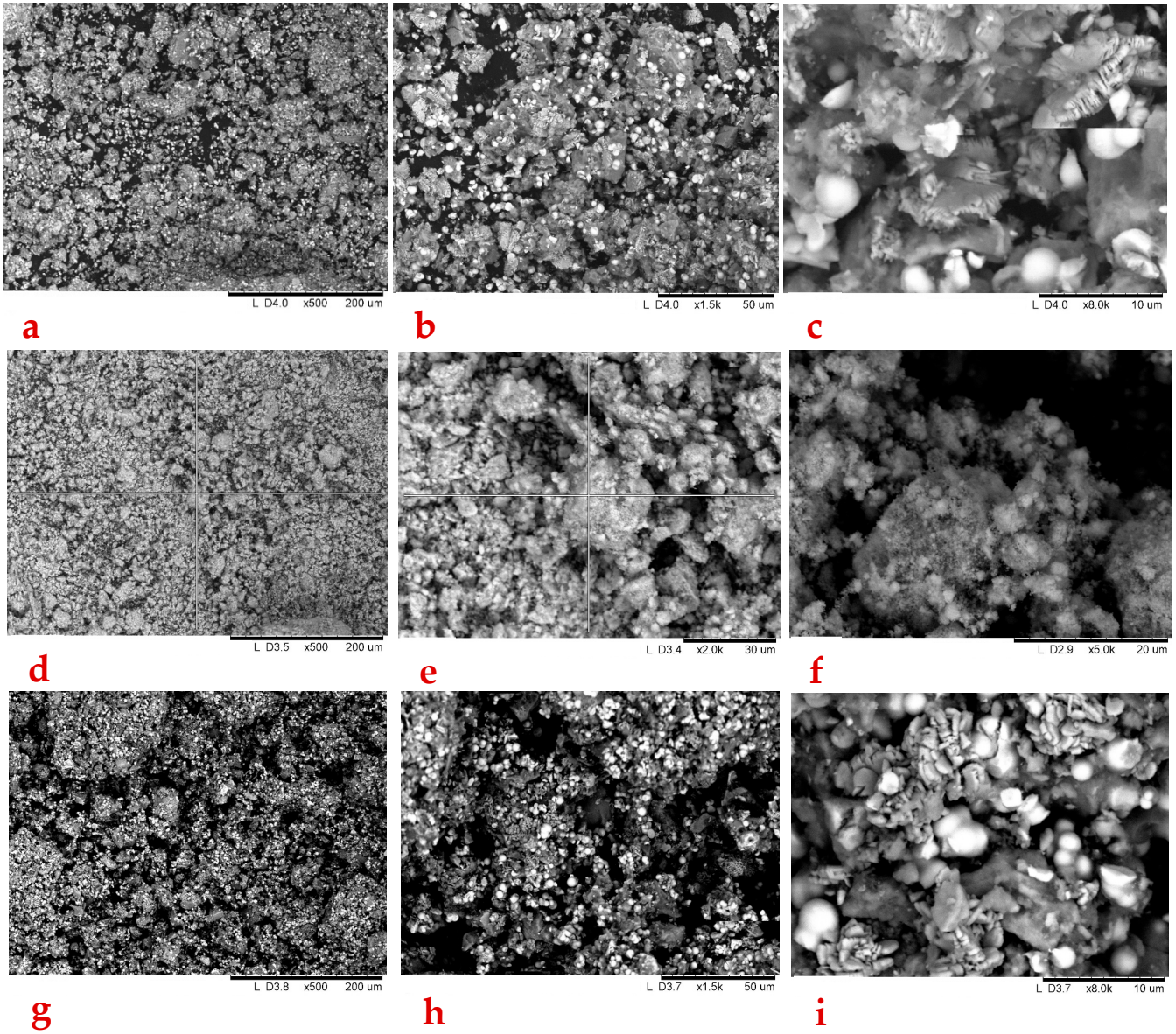

Figure 3. (**a**–**c**) SEM images of CU20%P-12 2°GEN with magnifications of ×500 (**a**), ×1500 (**b**), ×8000 (**c**); (**d**–**f**) SEM images of CU20%CERIA with magnifications of ×500 (**d**), ×2000 (**e**), ×5000 (**f**); (**g**–**i**) SEM images of CU20%WI-12 with magnifications of ×500 (**g**), ×1500 (**h**), ×8000 (**i**).

Agglomerates of particles were obtained with irregular shapes and some microns in size. Different particles were visible and uniformly dispersed. The contrast in brightness was less evident for the ceria-supported sample than for the lighter mixed ceria–alumina support. When the pictures were collected in backscattering mode, the brighter pictures can be ascribed to the heavier element, which in all cases is constituted by Ce. Qualitatively speaking, the ceria particles are mainly present in smaller round particles. In the case of mixed supports, the ceria phase segregation may be visible. The EDX analysis allowed for confirming the Al/Ce ratio and verifying the Cu loading, the latter reported in Table 2. Except in a few cases, the Cu loading was always much smaller than the nominal one, indicating a lower surface exposure of the active metal than of the support. Indeed, though EDX is not a genuinely surface technique, its subsurface penetration is not very high (i.e., in the micron range). EDX mapping of the Ni and Cu catalysts that showed the best activity are reported in Figures S3.34 and S3.35, respectively. Mapping of the active phase allowed for confirming the uniform distribution of the active phase on the support for both catalysts.

3.1.3. N_2 Physisorption Analysis

The physisorption isotherms were of type 2, denoting a small contribution of micropores, with a predominant contribution of mesopores. The hysteresis was almost absent for the CeO_2 supported catalysts, while it was large and extended over a wide p/p° range for the CeO_2/Al_2O_3 supports. Compared with the IUPAC classification, in most cases, it was resembling an H4-type hysteresis [35]. The BET surface areas of each catalyst are listed in Table 2, together with the calculated crystallite sizes and the EDX metal loading.

Figure 4 reports the N_2 physisorption analysis of the three catalysts that showed higher activity. All of the three catalysts showed type IV isotherms. A BJH diagram showing the pore-specific volume distribution is also reported in Figures S4.1–S4.4 of the Supplementary Materials file.

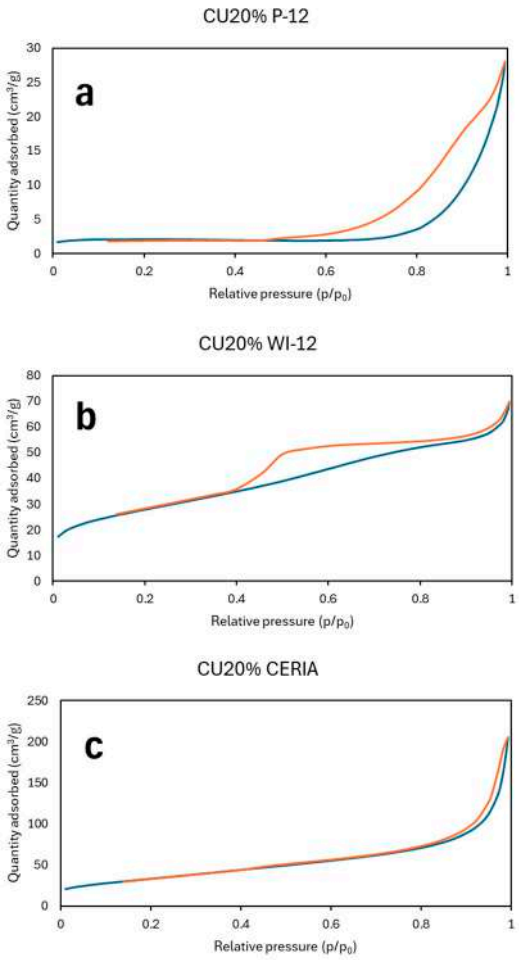

Figure 4. (**a**–**c**) N_2 physisorption analysis of CU20%P-12 (**a**), CU20%WI-12 (**b**), CU20%CERIA (**c**). Blue line for adsorption branch, orange line for desorption.

The specific surface area was very small when the coprecipitation was conducted with a carbonate alkaline solution (sample CU20%P-12 1°G) than with NaOH (all the other samples). On this basis, NaOH was selected as the precipitating agent for all the subsequent samples.

The surface area increased by raising the Al/Ce ratio, while it decreased during the impregnation of the support with the active metal (more with increasing Cu loading through WI).

3.1.4. Temperature-Programmed Reduction (TPR)

To better understand the activity difference due to the different preparation methods, temperature-programmed reductions (TPR) were performed over the three most active

catalysts. The TPR results are displayed in Figure 5. Detailed deconvolution plots of all of the analyses performed are reported in the Supplementary Materials.

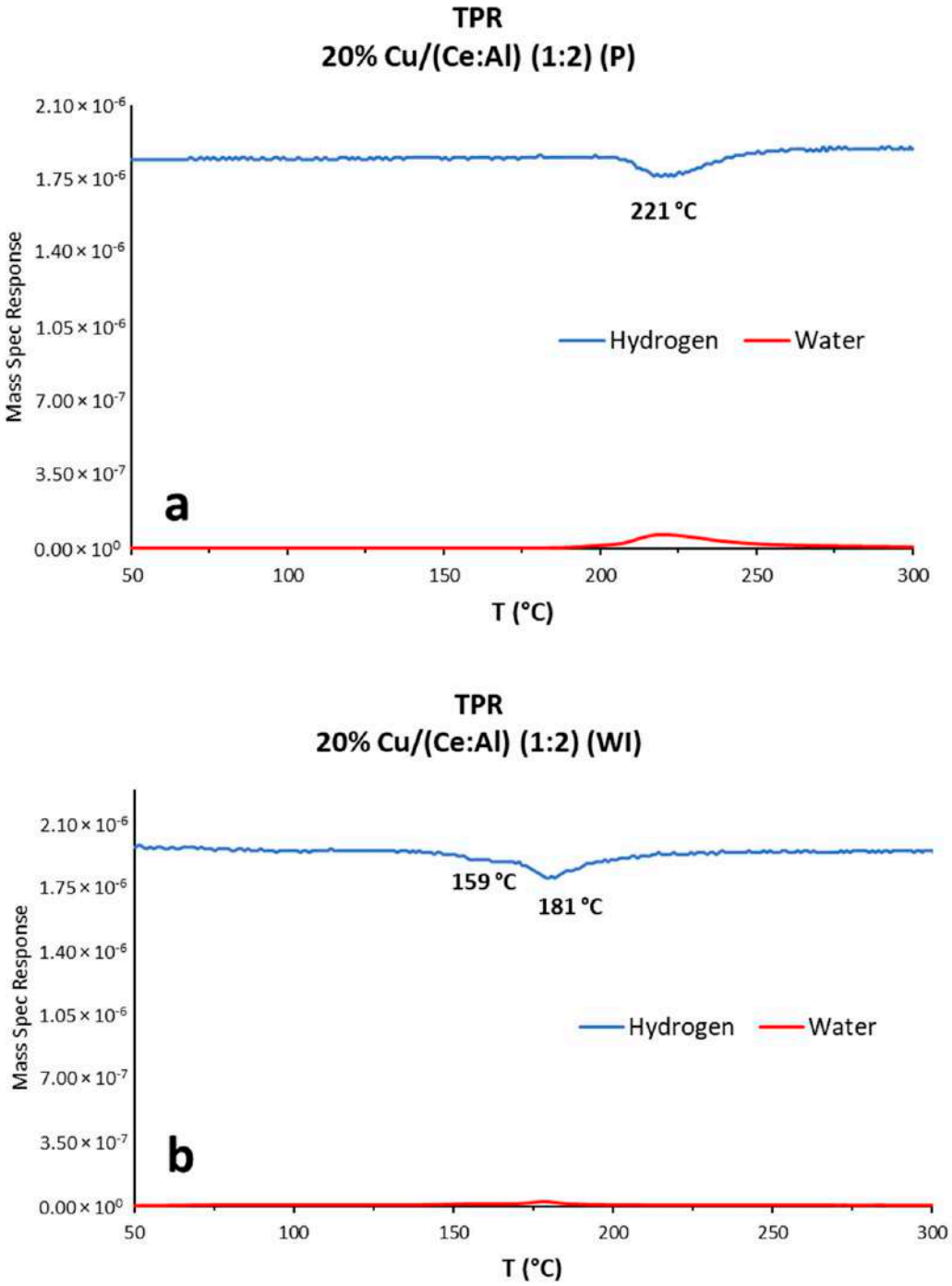

Figure 5. *Cont.*

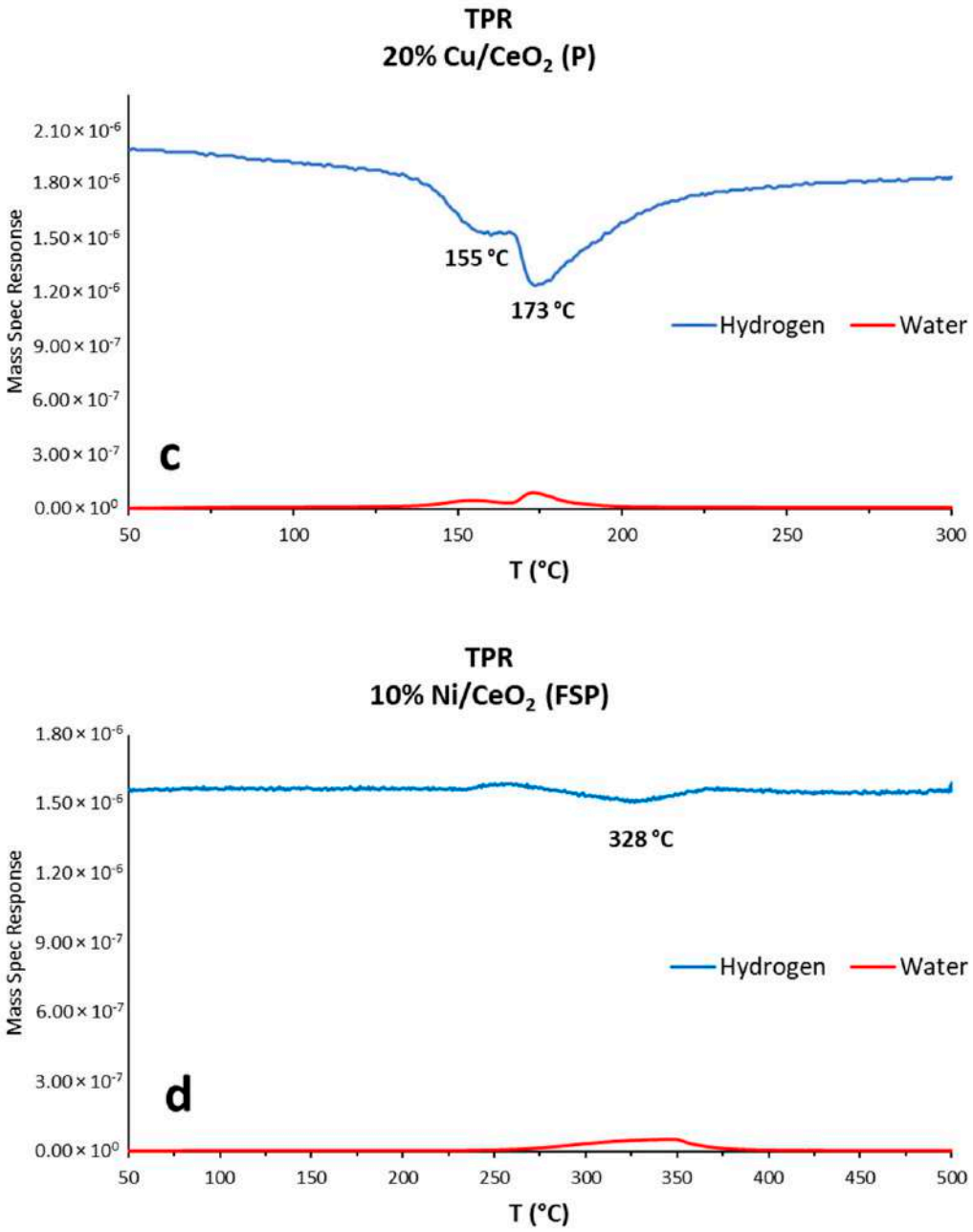

Figure 5. (**a**–**d**) TPR analysis of CU20%P–12 (**a**), CU20%WI–12 (**b**), CU20%CERIA (**c**), NI10%CERIA FPS (**d**).

Since in the case of Ni as the active phase, the activation prior to the analysis was performed at 350 °C, and H_2-TPRs at both 350 °C and 500 °C were performed. A TPR of the 10% Ni/CeO_2 FSP sample was performed at 500 °C and is reported in Figure 5d. Both analyses allowed us to obtain the same H_2 consumption value, demonstrating the actual reduction of the catalyst under the selected activation conditions.

A significant difference in the number of peaks and the reduction temperature of the different samples can be immediately observed from the analysis. The CU20%P-12 sample showed a single reduction peak at roughly 220 °C, with the lowest H_2 consumption among the three catalysts tested (86.1 micromoles H_2). The sample prepared by WI with the same metal loading (CU20%WI-12) showed two reduction peaks, both at lower temperatures than the previous sample (i.e., at 159 °C and 181 °C). The catalyst supported on CeO_2, even showed slightly lower reduction temperatures, with the peak maximums registered

at 155 °C and 173 °C. Furthermore, the CU20%WI-12 (b) and CU20%CERIA (c) samples led to higher hydrogen consumption (143 and 667 micromoles of H_2, respectively).

As reported in the literature, CeO_2 is reduced at a much higher temperature than those used in this TPR (roughly 540 °C for superficial CeO_2 and 840 °C for bulk cerium) [36,37]. Consequently, all reduction peaks below 350 °C can be attributed to copper species. The presence of one single peak, as in CU20%P-12, testifies that homogeneous CuO particles are present in the sample and that they undergo a direct one-step reduction to metallic Cu. Indeed, peak deconvolution resembles a single Gaussian peak (see Supplementary Materials). On the contrary, the presence of multiple peaks, as for the other two samples, may indicate either a non-homogeneous energy of interaction between CuO and the support, which may imply a different strength of the metal–support interaction, or a multistep reduction $Cu^{2+} \rightarrow Cu^{+}$ and then $\rightarrow Cu^{0}$. By deepening the analysis, the second peak at a higher temperature also includes a shoulder that evidences the presence of a third Cu^{n+} species, whose concentration is higher for CU20%CERIA than for CU20%WI-12.

The difference in the reduction peak temperature has been explained by different authors and is markedly different considering different metals. One of the most recognized, proposed by several authors, attributes the two reduction peaks, at high and low T, to large CuO particles and to finely dispersed CuO differently interacting with CeO_2, respectively [38–40]. Other authors consider the contribution of crystalline CuO particles, cluster Cu species, and isolated Cu^{2+} ions, as further explained later (vide infra) [41,42].

In these samples, the shift of the reduction temperature to lower values cannot be ascribed to the particle size, since it is similar for the CU20%WI-12 and CU20%P-12 (having different reduction temperatures), while the CuO particle size is significantly lower for CU20%CERIA, which has the same reduction temperature than CU20%WI-12.

The reducibility (and the opposite reduction temperature) of the three tested catalysts was in the same order of their catalytic activity, namely CU20%CERIA (c) > CU20%WI -12 (b) > CU20%P-12 (a). On this basis, a different explanation should be searched for as to the variation of the reduction temperature, attributing it predominantly to the interaction strength with the support. Stronger metal–support interaction leads to a higher reduction temperature and, thus, lower activity due to a possible inhibition of the redox cycle of the active metal. This is in line with similar findings for Ni based catalysts for other reforming reactions [43].

3.1.5. XPS Analysis

X-ray photoelectron spectroscopy (XPS) was also performed for surface analysis.

Characteristic copper peaks centered at 933.58 eV and 953.5 eV are visible in Figure 6. These peaks correspond, respectively, to Cu 2p 3/2 and Cu 2p 1/2. Satellite peaks at 942 eV are also present, due to Cu^{2+} species. The Cu 2p 3/2 is characteristically due to the presence of a CuO sublattice in the catalyst [44]. Area values of the Cu 2p 3/2 peak for the CU20%P-12, CU20%WI-12, and CU20%CERIA catalysts are, compared to all of the HR peaks, 50.8%, 59.9%, and 63.6%, respectively. This supports a higher surface exposure of the latter sample, followed by the one prepared by wet impregnation and, finally, by co-precipitation.

Peaks in the range of 932.3–934.6 eV are typical of CuO/CeO_2 catalysts. In general, Cu 2p 3/2 peaks at binding energy in the range of 933.1–932.2 eV and without any satellite peak are indicators of the presence of reduced copper species. In all of our catalysts, the presence of satellite peaks, together with a higher Cu 2p3/2 binding energy (CU20%P-12, CU20%WI-12, and CU20%CERIA showed a Cu 2p3/2 binding energy of 933.5 eV, 933.5 eV, and 933.7 eV) are attributed instead to CuO [45,46]. Even though the binding energies of Cu^{2+} and Cu^{+} are similar, the latter being 1 eV less only, peak deconvolution supports the presence of CuO on the as-prepared catalysts as the only copper species.

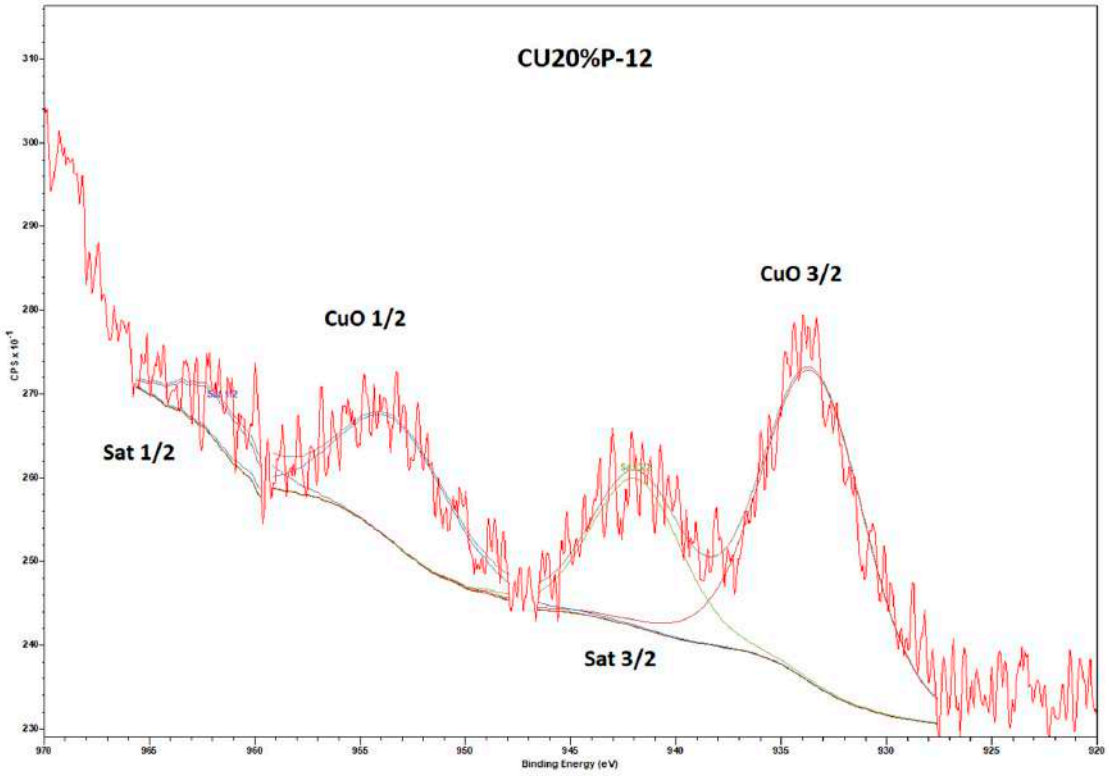

(**a**)

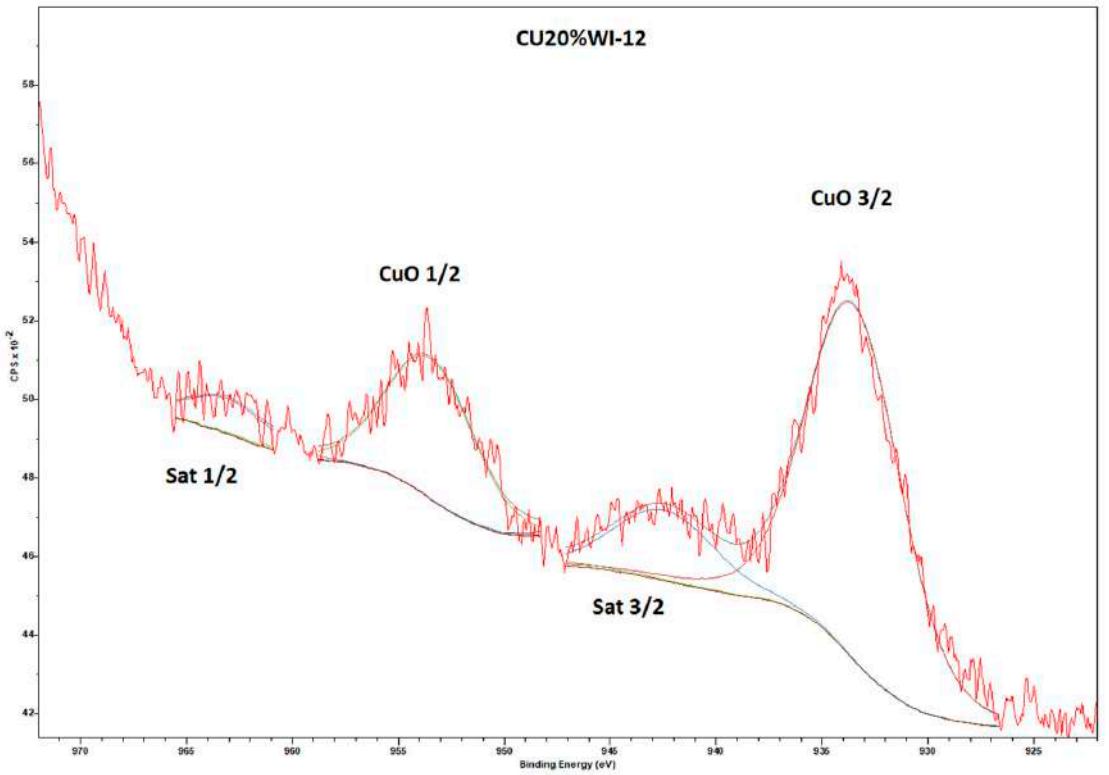

(**b**)

Figure 6. *Cont.*

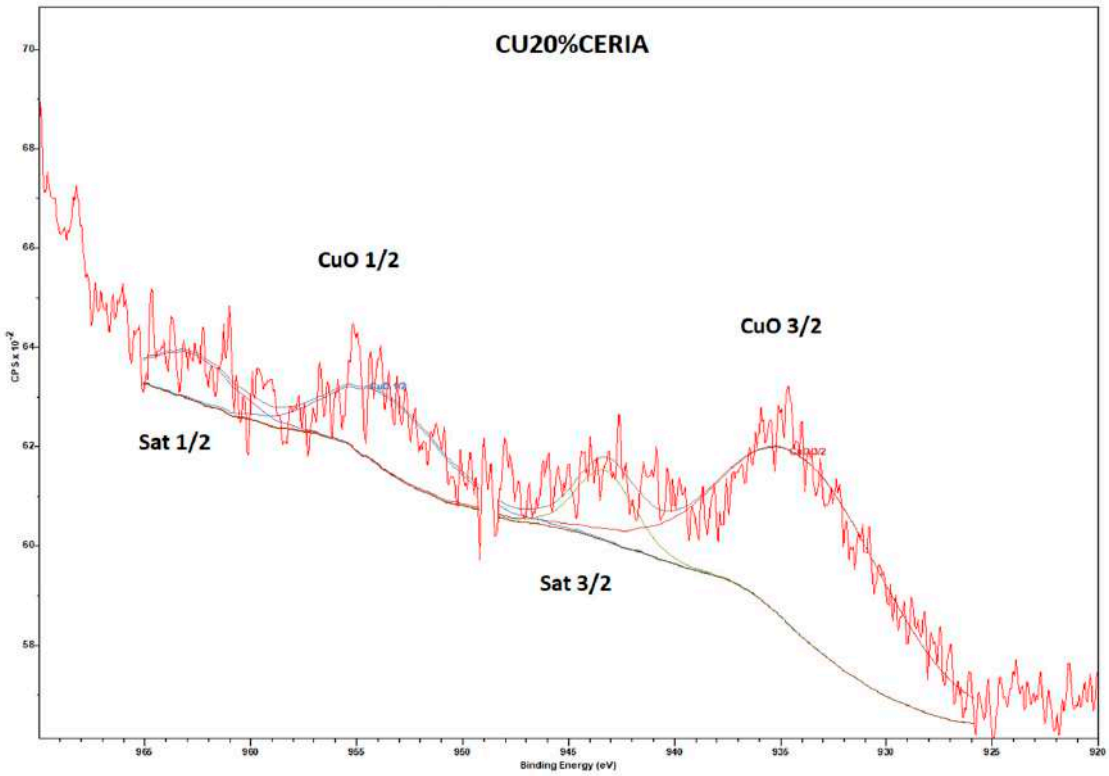

(**c**)

Figure 6. XPS analysis of CU20%P-12 (**a**), CU20%WI-12 (**b**), CU20%CERIA (**c**).

3.2. Activity Testing

Every catalyst has been tested twice, and the results averaged.

A blank test without any catalyst (carborundum 0.9 g was the only solid material filling the reactor) was performed to evaluate the methanol conversion at different temperatures and the possible hydrogen formation due to a homogeneous reaction.

The results of blank tests are summarized in Table 3. While low-temperature conversion was visible, mainly due to methanol oxidation, the hydrogen yield was negligible, even at the highest temperature. Traces of methane and acetaldehyde were occasionally found, with the latter ascribed to a limited oxidative coupling of the reactant.

Table 3. Blank activity testing at different temperatures.

T (°C)	MeOH Conversion	H_2 Yield	CO_2/CO_x Ratio	Impurity
200 °C	18.19%	/	/	CH_3CHO
230 °C	36.55%	/	/	CH_3CHO
260 °C	25.99%	/	/	/
280 °C	12.72%	0.72%	41.96–58.04%	/
300 °C	18.88%	1.46%	57.39–42.61%	/
320 °C	30.52%	1.90%	42.57–57.43%	$CH_3CHO + CH_4$
340 °C	26.42%	1.78%	45.80–54.20%	CH_3CHO
360 °C	30.07%	2.47%	47.23–52.77%	$CH_3CHO + CH_4$
390 °C	30.63%	2.97%	47.75–52.25%	$CH_3CHO + CH_4$
410 °C	31.19%	3.24%	46.14–53.86%	$CH_3CHO + CH_4$

3.2.1. Copper-Based Catalysts

The first choice was to co-precipitate the active phase and the support, which was, in turn, constituted by a mixed ceria–alumina oxide. Two precipitating agents were compared.

First was sodium carbonate (first-generation catalyst) to achieve a milder and more gradual variation of pH, and the second choice was NaOH. A much smaller surface area was achieved while using the carbonate, and this resulted in poor methanol conversion, reaching a maximum of 60% at the highest temperature and, correspondingly, a very modest hydrogen yield (ca. 15%), Figure 7. Changing the precipitating agent to NaOH considerably increased the surface area of the catalyst (i.e., from 6 to 49 m^2/g, Table 2) and improved both methanol conversion (to 100% at 390 °C) and H_2 yield (to ca. 60–70% at a temperature higher than 340 °C). A first hypothesis may be ascribed to improved dispersion of Cu over a higher surface area catalyst. Nevertheless, halving the metal loading (in principle increasing the metal dispersion) was not effective in further improving the activity, since methanol conversion and H_2 yield leveled off at ca. 70% and 35%, respectively.

(**a**)

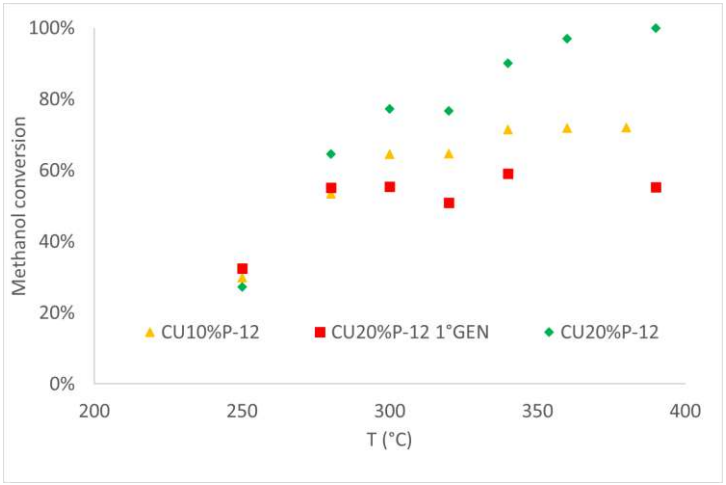

(**b**)

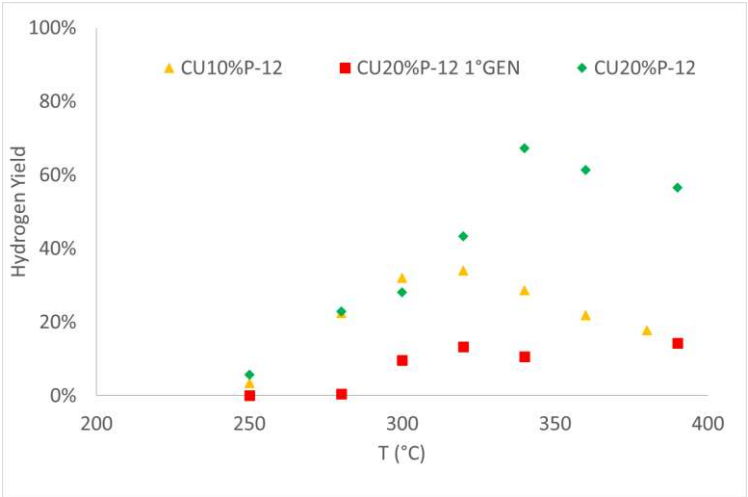

Figure 7. (**a**) Methanol conversion and (**b**) hydrogen yield vs. temperature for Cu loaded catalysts obtained by co-precipitation.

Many authors have tested high Cu loadings for the OSRM reaction, showing that, for the same preparation method, catalytic activity increases as Cu loading increases. Udani et al. investigated the role of Cu loading in OSRM over a series of co-precipitated CuO/CeO_2 catalysts [47], reporting a slight increase in catalyst activity as Cu loading increases, despite the decreased dispersion, as shown by H_2-TPR.

Furthermore, with the simultaneous co-precipitation of the active phase and the support, Cu remains partly inaccessible to the reactants in the solid particle.

To check this point, different preparation methods were compared, while keeping the same 20% metal loading (Figure 8). The catalysts obtained by impregnation of the Ce-Al support showed a much higher surface area, ca. doubled. On the contrary, lower real loading than the nominal was obtained after impregnation, with respect to co-precipitation. Both methanol conversion and hydrogen yield were higher for the samples obtained by wet impregnation than by precipitation, likely thanks to a better surface availability of the active metal, as shown by XPS analysis in Figure 8. Indeed, the Cu 2p 3/2 peak reported for the CU20%P-12 (a) and CU20%WI-12 (b) showed 50.8% and 59.9%, respectively.

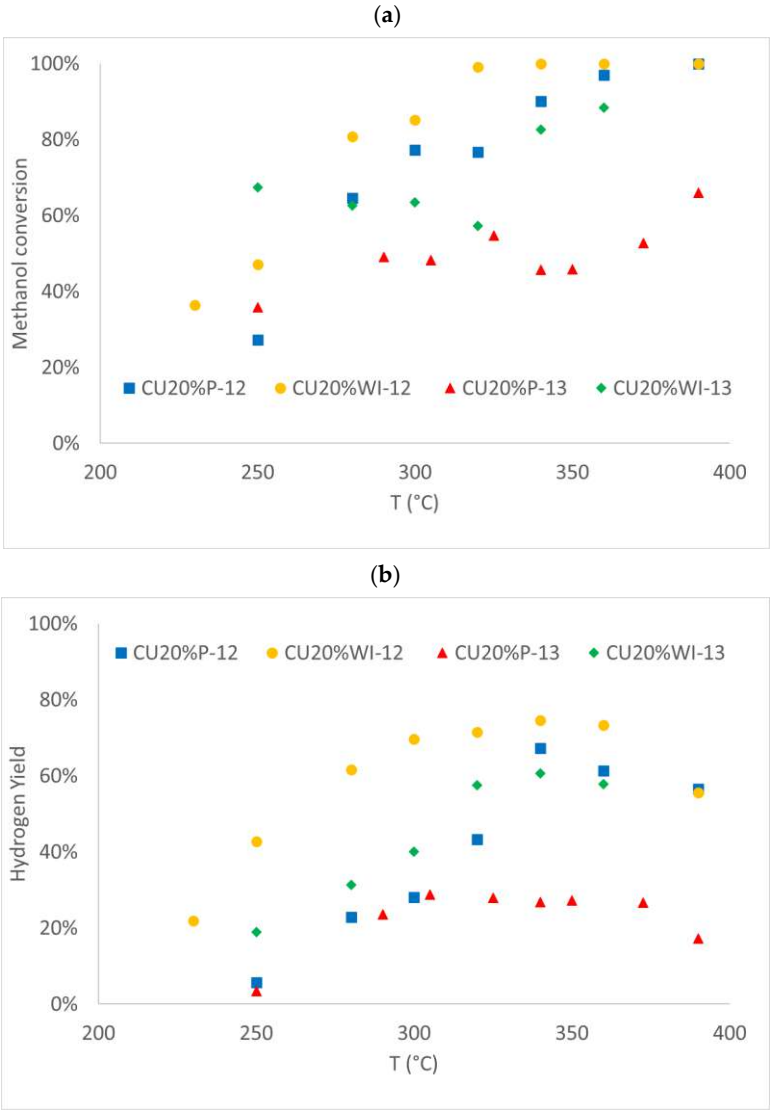

Figure 8. (**a**) Methanol conversion and (**b**) hydrogen yield vs. temperature for Cu 20 wt% loaded on ceria alumina (1:2 or 1:3 mol/mol). Active metal added by co-precipitation or by wet impregnation.

Surface exposure and dispersion at high metal loading can be increased by using higher surface area supports. Therefore, the content of alumina was modified. Alumina in these catalysts primarily contributes through a physical role. High surface area and high porosity are widely recognized as some of the most attractive properties of alumina. As expected, an increase in the alumina content in the mixed oxide support led to an increase in surface area, but it was detrimental to activity. This effect was observed in both the co-precipitation and wet-impregnation preparation procedures when diluting the ceria 1:2 or 1:3 mol/mol with alumina.

While the effect of support acidity is not considered significant in the literature, the redox properties of the catalyst are central to determining the performance.

For instance, according to Zou et al., when CuO is present on the ceria, the support significantly alters the redox properties of the catalyst. The strong interaction between CuO and CeO_2, known as strong metal–support interaction (SMSI), is believed to cause changes in the reduction temperature of the catalyst [36,41], as appreciated in Figure 5, impacting the activity as well. Authors report that Cu^+ species may result from the strong interaction of CuO clusters with CeO_2. At the interface between copper oxide and ceria, Ce^{4+} was replaced with Cu^+ due to the practically identical ionic radius values of the two. As a result of the SMSI between CuO and CeO_2, the Cu_xO/CeO_2-y catalysts had an altered Ce^{4+}/Ce^{3+} and Cu^{2+}/Cu^+ redox pair concentration [46]. This can modify the ability of the catalyst to oxidize the reactant.

Yet, the higher activity of the wet-impregnation metal-loading method vs. co-precipitation was confirmed also for the ceria–alumina 1:3 sample.

When looking at the CO_2/CO ratio, with the aim of keeping it as maximum as possible, all the catalysts returned to a decreasing ratio between the two species with increasing temperature. Some samples showed much higher CO_2/CO at a low temperature, due to higher oxidative activity and better performance for the water gas shift reaction ($CO + H_2O \leftrightarrows CO_2 + H_2$, which is exothermic, so favored at low temperature). In particular, 20 wt% Cu loading showed the best compromise also for this aspect, since with this loading the highest CO_2/CO ratio was achieved irrespective of the support composition and the preparation method. Regarding the latter aspect, however, the co-precipitation method allowed us to obtain a higher CO_2 yield with respect to the samples prepared by wet impregnation. This is likely due to the oxygen-buffer effect of CeO_2, which is important to increase the oxidating activity also mediated by the support. The impregnation procedure leads to higher metal surface exposure with respect to the support. If this can be beneficial for activity, the selectivity towards full oxidation, which takes advantage of the oxidative power of ceria, is disfavored by lower support exposure.

Matching all these aspects, a new set of samples supported over CeO_2 only was prepared, to check also the effect of further increasing the Cu concentration. The results are reported in Figure 9 and further confirmed that 20 wt% Cu loading was the best choice over higher values for both the supports. In particular, full methanol conversion was achieved at 280 °C for the pure ceria support and at 320 °C for the ceria–alumina support, respectively, and the maximum H_2 yield was ca. 80% and ca. 75%, respectively. This elected CeO_2 as the most interesting support of this series.

3.2.2. Nickel-Based Catalyst

Another class of catalyst tested is the one composed of nickel supported over CeO_2 or CeO_2/Al_2O_3. Ni is very well known as a catalyst for the steam reforming of various substrates and a comparison between these two different active phases may highlight their different role. In this case, previous results suggested checking an alternative method of preparation, which returned very active and stable catalysts for the steam reforming of ethanol [23,27]. In particular, it was demonstrated that Ni-based catalysts prepared over various supports by flame spray pyrolysis (FSP) resulted in more activity than samples prepared by wet impregnation and by co-precipitation. Furthermore, higher dispersion of the metal and stronger metal–support interaction were demonstrated for the FSP-prepared samples, and this contributed to higher activity and much better resistance of the catalyst towards deactivation by coking. These aspects were less evident for the Cu-based samples, as detailed in the Section 2.

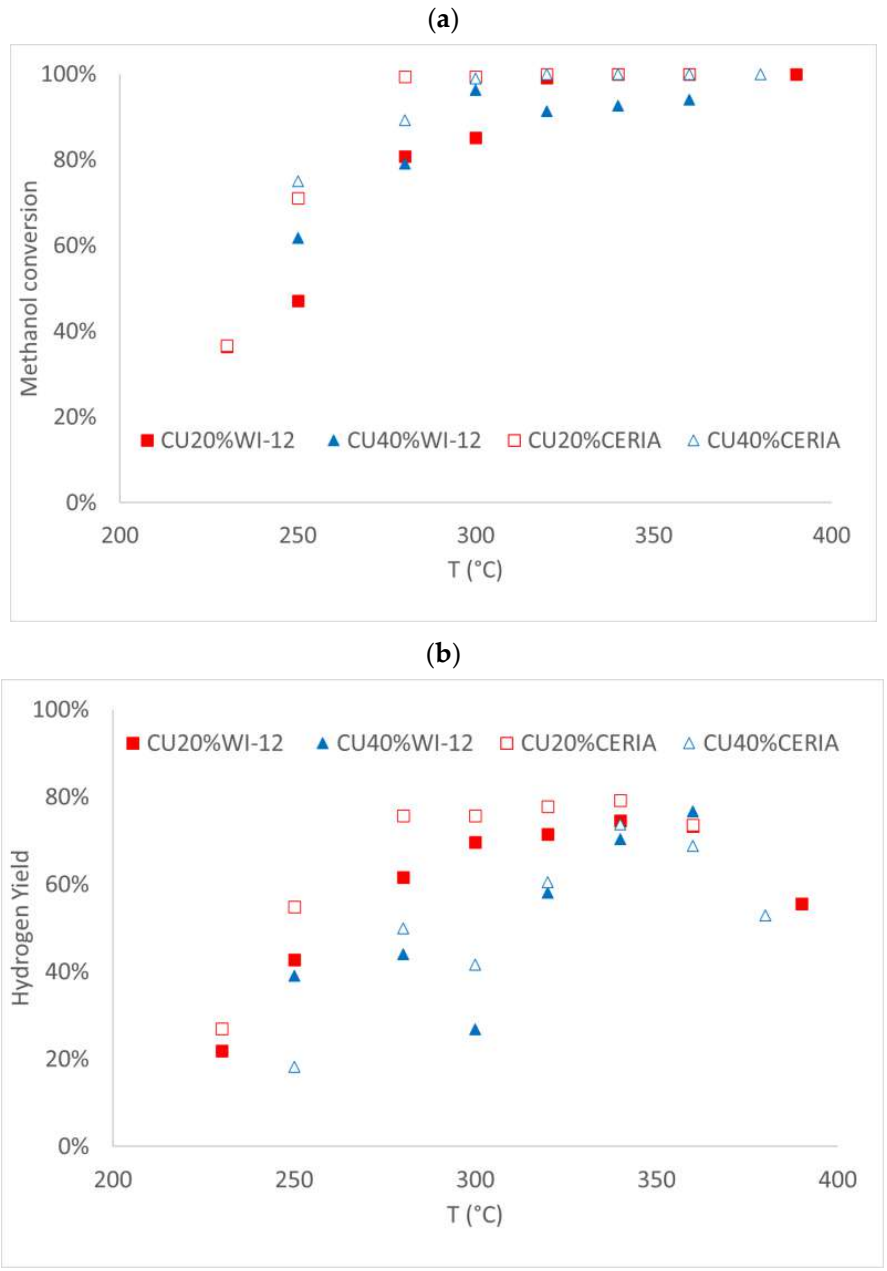

Figure 9. (**a**) Methanol conversion and (**b**) hydrogen yield vs. temperature for Cu 20–40 wt% loaded on ceria–alumina (1:2) and on CeO_2.

The catalyst prepared with the FSP method with a 10 wt% of nickel content supported over CeO_2 presented a lower surface area than the respective copper-based catalyst. FSP guarantees, however, a great degree of crystallinity, as shown in the XRD diffractograms reported in the Supplementary Materials.

The methanol conversion was high even at a low temperature and so was the hydrogen yield, even if it was constantly lower than that of the Cu/CeO_2 samples (Figure 10). Lower Ni content than Cu led to higher activity. Indeed, the sample NI10%FSP achieved ca. 100% methanol conversion at 320 °C with a ca. 63% H_2 yield. Both parameters decreased either by increasing the metal loading or when preparing the sample by impregnation.

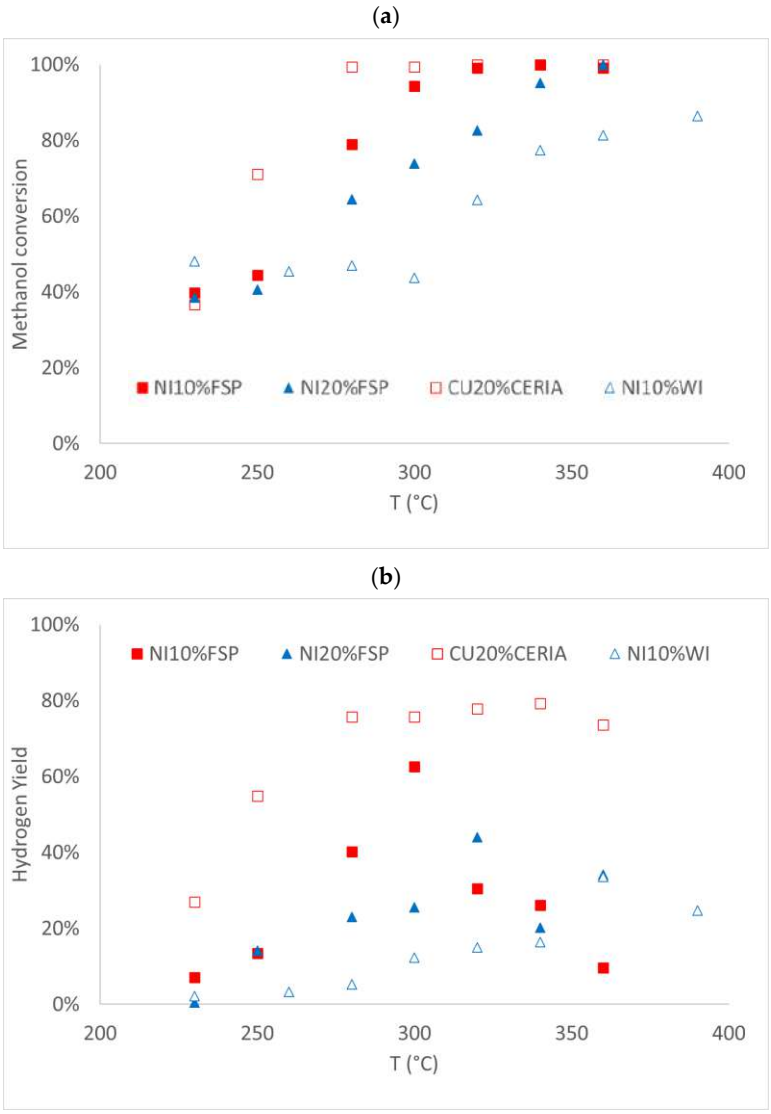

Figure 10. (**a**) Methanol conversion and (**b**) hydrogen yield vs. temperature for Ni-based catalysts loaded on ceria.

Another interesting feature is that at a temperature close to 300 °C, the methanation process started to become very competitive, the hydrogen yield decreased, and the methane formation became predominant with the Ni-based catalyst. The methanation process showed to be predominant with the increase in temperature but remained negligible below 280 °C. The nickel efficiency in the methanation process is indeed very well-known, and the ceria support seems to amplify this pathway [48].

The hydrogen yield at 300 °C was in many cases higher for Ni than with many Cu-based catalysts, and the co-presence of methane can produce anyway an interesting fuel mixture.

The ratio between CO_2/CO was also much higher in the whole range of temperatures than with most of the Cu-based samples, which is another interesting feature.

NI20%FSP presented minor activity, both in terms of hydrogen yield and methanation, despite the bigger surface area and the same degree of crystallinity as sample NI10%FSP. The methanation reaction, following the same behavior of the previous catalyst, improved with the temperature but slower than with NI10%FSP. This can be due to the lower effect of the ceria sites at higher Ni loading. Both catalysts returned higher selectivity to CO_2 than CO over the whole temperature range, with respect to the Cu-based samples.

Finally, the catalyst prepared by the wet-impregnation method with a 10 wt% nickel loading supported over CeO_2 returned a much higher surface area but lower crystallinity. Indeed, the crystal size of the Ni particles was not retrievable from the XRD data. The sample was characterized by much lower methanol conversion, which was unable to reach 100% even at 390 °C. Correspondingly, the hydrogen yield was very limited, reaching a maximum of 25%, but surprisingly also, the methane yield was much lower than for the FSP-prepared materials. Indeed, in this case, the main byproduct was acetaldehyde. The decrease of both methane and acetaldehyde (and hydrogen) yields at the highest temperature was attributed to a prevailing oxidative activity because it was accompanied by a simultaneous increase in the CO_2/CO ratio. Acetaldehyde and methane yields are also reported for completeness in Figure 11.

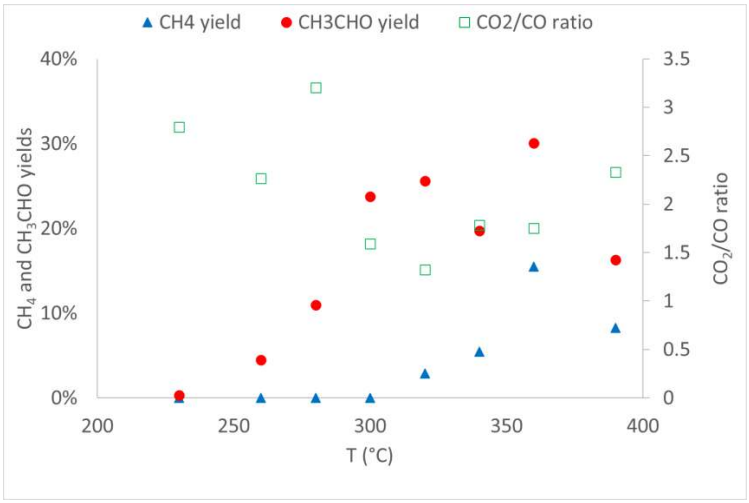

Figure 11. Acetaldehyde and methane yields (left axis) and CO_2/CO ratio (right axis) vs. temperature.

3.2.3. Durability Test

The results of a durability test on the most active catalyst (CU20%CERIA) are reported in Figure 12. The test was carried out by keeping the sample for ca. 220 h at the temperature of 280 °C, i.e., the conditions of 100% conversion and maximum H_2 yield. The conversion remained within 99–100% for the whole testing time, confirming the stability of the material, at least for the duration of the test, after a slight loss of activity in the very first h on-stream.

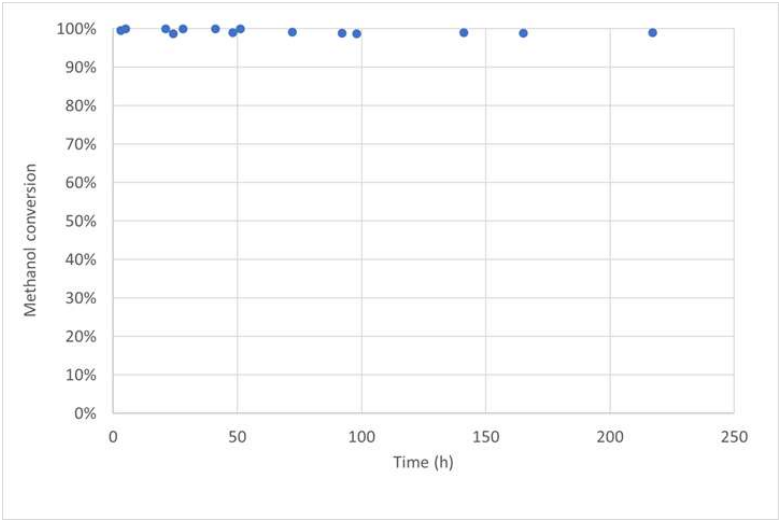

Figure 12. Durability test for the catalyst CU20%CERIA.

4. Discussion

The degree of crystallinity and the surface area often influence the catalytic activity. This is correlated to the methodology used in the synthesis. Wet impregnation usually led to significant available surface area, even covering the pores with the active phase of copper or nickel, and this led to a generally higher activity than the samples prepared by co-precipitation, especially when a high surface area oxide was added as support, such as alumina. The co-precipitation method leads usually to an intermediate surface area, but it was more difficult to achieve high crystallinity with this methodology.

The ratio between ceria and alumina was studied using different molar proportions. A lower alumina content was better, since the performances of catalysts with a 1:2 molar ratio were in general better than for a 1:3 dilution ratio, with a greater hydrogen yield, in particular in the co-precipitation case. The catalyst produced without alumina (CU20%CERIA) was the most active due to multiple causes. First of all, the ceria plays a key role in facilitating the adsorption/desorption of oxygen species, as an oxygen buffer, and in general, improves the activity when used as a co-catalyst. Furthermore, the synthesis of CU20%CERIA allowed us to obtain a catalyst with a higher surface exposure of smaller CuO particles, as evidenced by the XPS and XRD analyses.

This supports a synergistic effect in this reaction between Cu and CeO_2. Indeed, ceria is often reported as a non-innocent support for most of its applications. The redox behaviors of each species, Cu-CuO and CeO_x-CeO_2, are often suggested to be interlinked, allowing ceria-supported copper domains to outperform copper species on other, non-redox active supports. For instance, this was demonstrated in the reversible conversion of CO_2 to CO [49], for NO_x conversion with CO [50,51], and for the reverse water–gas shift reaction [52]

A controversial point is the effect of particle size and dispersion and different crystal facets on the activity of methanol steam and oxy-steam reforming. Also, this point is correlated to the preparation method and in turn, to the interaction strength with the support. According to some studies, the highly dispersed CuO strongly interacts with CeO_2, and this interaction leads to a change in the reduction temperature of the CuO and can be linked to an increase in the activity of the catalyst. It is often reported that bulk CuO is much less reducible than finely dispersed CuO [39,41,47]. High-temperature peaks in the TPR (at less than 500 °C, excluding the CeO_2 partial reduction) are, therefore, assigned in some of the literature to large CuO bulk particles, poorly interacting with the support, while small CuO particles, strongly interacting with the support, would be reduced at lower temperature.

The difference in the reduction temperatures of the present catalysts is well evident from the H_2-TPR analysis reported in Figure 5. By comparing these data with the XRD ones (Table 2), one may infer that the same average particle size of CuO is achieved for the catalyst supported over ceria–alumina, either prepared by coprecipitation or by incipient wetness (27–28 nm). On the contrary, a much lower reduction temperature was achieved for the sample prepared by impregnation than by precipitation. In addition, only one reduction peak was observed for the latter, while after impregnation, apparently, three different copper species are present, reducing at different temperatures. The XPS data do not reveal a significant presence of Cu_2O, so the different reduction peaks are ascribed to the reduction of CuO as the starting material, with inhomogeneous metal–support interaction strength. For the sample prepared by co-precipitation with ceria–alumina very homogeneous species are present, there is a relatively small interval in the reduction temperature and a peak deconvolution that is compatible with a single Gaussian curve, as reported in the Supplementary Materials File. It can be concluded that the co-precipitation procedure brings the fine and homogeneous incorporation of CuO into the support and that its reduction leads to Cu in one reduction stage.

The wet-impregnation procedure led to similar CuO particle size but with less homogeneous interaction strength with the support, which ended in three different reduction features, with a predominant concentration of intermediately reducing species and with

a general higher reducibility. The same three reducing species were observed when the support was ceria, though their concentration on the catalyst was a more similar one to the other (see TPR peaks deconvolution in the Supplementary Materials File), and the particle size was much lower.

On the basis of this evidence, we can attribute the low-temperature reduction features to predominantly surface species (surface exposure of CuO was higher for the sample prepared by WI and for the CeO_2 supported sample, and in particular, by comparing these latter samples, it can be concluded that CuO species reducing at ca. 188 °C can be correlated to the higher activity achieved when using pure ceria as support. These species are characterized by an intermediate metal–support interaction strength. This partially contradicts what is reported in the above-cited literature (which attributes low reduction temperature to strongly interacting metal–support systems [40]), but it resembles what is widely reported for Ni supported particles, whose high dispersion and strong metal–support interaction (and high activity) are indeed connected with a high reduction temperature [43].

The copper content has a notable effect on the hydrogen yield but also on the CO_2/CO ratio and in the production of by-products. The 40% copper content and the 20% copper content have almost the same hydrogen production. The 40% has the downside of having a larger production of carbon monoxide at a lower temperature than the 20% copper content and the production of methane and acetaldehyde that are not present at a lower copper content. This is probably due to the fact that the excess of copper in the catalyst surface in the 40% case mostly covers the ceria and by that facilitates the methanol decomposition and the methanol conversion into other species rather than the methanol oxidation to CO_2, the results of which are improved by the presence of ceria. The 10% copper content, on the other hand, has almost no production of by-products even at 400 °C, but the methanol conversion and the hydrogen yield were significantly lower.

The nickel-based catalysts clearly show how the flame spray pyrolysis can synthetize a much better catalyst than the wet-impregnation method with this active phase. The crystallinity, the surface area, the homogeneity of the particles observed with SEM, and of course, the final activities were significantly better for the two FSP catalyst than the WI one. Unfortunately, the FSP preparation procedure did not work as well for the preparation of Cu-based catalysts, as discussed elsewhere [23,27].

The Ni-containing catalysts were generally active at a lower temperature than the copper ones, but by increasing the temperature, the methanation reaction slowly became predominant. This is not necessarily a problem if the goal is just to obtain a mix of combustible gases. But, to achieve hydrogen to be sent to a fuel cell, this is certainly an issue.

Table 4 reports a comparison between the present catalysts and some of the most interesting examples reported in the literature.

From what is reported in [8], the best metal loading was between 5 and 20 wt%, with the activity decreasing by increasing further the metal concentration. The temperature used was slightly lower than the one in the present work, but the hydrogen yield was generally lower. For instance, the catalyst CU20%WI-12 has a maximum hydrogen selectivity of 69.40%, with a methanol conversion of 100%, which is a bit higher than the 68.20% presented in the literature. The same holds for sample CU40%WI-13 with a H_2 yield of 69.29% at full methanol conversion.

By using a different support and removing the alumina, the working temperature was reduced significantly. Cu20%CERIA and Cu40%CERIA reached the highest conversion between 280 and 300 °C, which are closer to the literature ones. The hydrogen selectivity for these two catalysts was 68.52% and 68.01%, respectively.

Table 4. Comparison of the catalytic performance of similar samples found in the literature. WI = wet impregnation; DP = deposition–precipitation; SIP = subsequent impregnation; CP = co-precipitation.

Catalyst	Prep. Method	SBET (m^2/g)	Red. T (°C)	Red. Time (h)	GHSV (h^{-1})	T OSRM (°C)	CH_3OH Conv. (%)	H_2 Selectivity (%)
Cu (5)/CeO_2/Al_2O_3 [8]	WI	126	300	1	26,700	250	97.7	69.1
Cu (20)/CeO_2/Al_2O_3 [8]	WI	101	300	1	26,700	250	99.6	68.2
Cu (40)/CeO_2/Al_2O_3 [8]	WI	90	300	1	26,700	250	87.9	65.7
Cu (60)/CeO_2/Al_2O_3 [8]	WI	30	300	1	26,700	250	9.6	28.5
Ni (5)/CeO_2/Al_2O_3 [53]	WI	132	300	1	26,700	250	2	30.5
Ni (20)/CeO_2/Al_2O_3 [53]	WI	128	300	1	26,700	250	31	33
Ni (40)/CeO_2/Al_2O_3 [53]	WI	78	300	1	26,700	250	98	68.9
Ni (60)/CeO_2/Al_2O_3 [53]	WI	133	300	1	26,700	250	77	58.2
Ni (40)/CeO_2 [53]	WI	34	300	1	26,700	250	85	68.6
Cu-Ni/ZrO_2 [54]	DP	35	300	1	30,000	250	55	60.0
Cu (30%)-Ni(10%)/ZrO_2/Al_2O_3 [55]	SIP	119	300	1	/	200	87	69.49
Cu (30%)-Ni(10%)/CeO_2/Al_2O_3 [55]	SIP	134	300	1	/	200	98	69.17
Pd (0.5)-Ni (20)/ZnO/Al_2O_3 [56]	SIP	106	300	1	26,700	300	99.0	73.0
Au (1.0)-Cu (20)/MWCNTs [57]	DP	272	300	1	26,700	300	83.0	73.0
Au (1.0)-Ni (20)/MWCNTs [58]	DP	311	300	1	26,700	300	99.8	70.4
Au-Cu (Au/Cu = 3/1) (5%) /$Ce_{0.75}Zr_{0.25}O_2$ [59]	CP	143	300	1	/	350	99.6	62.4
Cu (20%)/CeO_2/Al_2O_3 (1:2) [This work]	WI	95	300	1	23,500	340	100	74.5
Cu (20%)/CeO_2 [This work]	CP	121	300	1	26,500	280	100	75.7
Ni (10%)/CeO_2 [This work]	FSP	9	300	1	27,900	300	100	62.5

Regarding the nickel catalysts, the literature comparison confirms in general a worse performance with respect to Cu, and that by increasing the nickel content in the catalyst, the methanol conversion and the hydrogen selectivity increase until 40 wt% Ni loading. In the present work, a much lower Ni content was needed, i.e., 10 wt%, to achieve 99% conversion, but the main problem was the selectivity, mainly to CH_4, which increased at increasing metal loading. Bi-metallic formulations have been also proposed, with the main advantage of decreasing the operating temperature, without significant improvement of the conversion and hydrogen yield. The high efficiency and the lower temperature at which these catalysts are active could be explained by the formation of the $Cu_{0.8}$-$Ni_{0.2}$ metal alloy on the catalyst surface, which is active even below 200 °C. One of the possible downsides, highlighted in the literature, of copper–nickel catalysts is the formation of a great quantity of CO. The CO/CO_2 selectivity in Cu (30%)-Ni(10%)/$CeO_2Al_2O_3$, for example, is 95% [55].

In the literature are also presented some catalysts that exceed the hydrogen yield obtained in this work, but they are usually composed of a bi-metallic catalyst with a noble metal incorporated in the active phase, usually gold or platinum. Furthermore, the stability of these catalysts is not reported in the papers.

Different mechanisms of reaction have been proposed for this reaction, which involves a wide pool of intermediate and elementary steps. Different authors are in broad disagreement on the pathways and even on the active species. For instance, Cu^{2+} is considered active only for the oxidation of methanol, while Cu^0 would be active for H_2 production. This interplay between different oxidation states is active in different phases of the reaction, since when oxygen is present, Cu is in its oxidized form. Meanwhile, the products of the reaction are reducing species, which restore the active metal in the reduced form [60,61]. In the present samples, after reduction, only Ni^0 and Cu^0 species were observed.

Various surface intermediate species have been detected on copper-based catalysts. This includes methoxy species, formaldehyde, diozymethylene, and formate, which can be mono or bi-dentate. Dissociative adsorption to methoxy species is considered by many

authors to be the first step of the reaction [61,62]. Partial oxygen exposure is needed to activate the catalyst. Wachs and Madix found that covering 20% of the surface with oxygen is necessary to maximize methanol adsorption [62]. Specific interaction between the hydroxyl end of the methanol molecule and an oxygen atom on the surface strongly improves the dissociative chemisorption step. A dehydrogenation step of the methoxy species leading to formaldehyde formation is widely accepted and identified as the rate-determining step of the reaction [63,64]. Formate species are also commonly observed during the adsorption of methanol, but even here, several authors disagree on the origin. Disproportionation of formaldehyde into methoxy species and formates [65], as well as dioxymethylene species dehydrogenation, have been proposed [66].

5. Conclusions

In this work, several catalysts based on Cu and Ni were supported over Ce-based supports, either pure or mixed with different amounts of alumina (1:2 and 1:3 mol/mol). Different metal loadings (10–40 wt%) and preparation methods (wet impregnation, co-precipitation, and FSP) were compared, leading to different surface area, crystallinity, CuO particle size, and interaction strength with the support. All the catalysts synthesized have been characterized through XRD, BET, SEM, EDX, TPR, and XPS and have been successfully tested for the oxidative steam reforming of methanol.

Every catalyst succeeded in increasing the methanol conversion with respect to the blank test. The hydrogen yield and the methanol conversion were strictly correlated with temperature, metal content, crystallinity of the catalyst particles, and the total surface area. Furthermore, the formation of copper species moderately interacting with the support was considered pivotal to increasing the activity and selectivity of the material. The formation of undesired products has been often observed, and the properties of the catalyst were tuned to maximize hydrogen selectivity while reducing carbon monoxide, methane, and acetaldehyde as by-products.

The best copper loading was 20 wt%, while the presence of increasing alumina was detrimental because the pure ceria support presented a higher hydrogen yield at lower temperatures.

Overall, smaller CuO and Cu particle sizes, higher reducibility, and surface exposure were achieved with the pure CeO_2 support, leading to the highest activity.

The nickel catalysts were very active in methanol conversion but presented the downside of being also active in the methanation reaction, which at relatively high temperatures decreased the formation of hydrogen and increased methane production.

In this regard, it can be said that copper is the best active phase and that ceria is definitely the best support for an OSRM reaction within this set of samples. Copper catalysts are cheap, easy to synthesize, and stable for a long period of time.

In conclusion, all the tests confirmed the great potential of the oxidative steam reforming of methanol to produce hydrogen at a relatively low temperature with the catalysts tested. The catalysts produced are easily implemented in industrial plants as pellets or as a powder; are easily manufactured, even on an industrial scale; and have proven to be durable for hundreds of hours on the testing range.

Supplementary Materials: The supporting information can be downloaded at https://www.mdpi.com/article/10.3390/catal14110759/s1.

Author Contributions: Conceptualization, I.R. and G.R.; methodology, D.C.; validation, M.T., S.N.D. and A.G.; formal analysis, M.T. and A.G.; investigation, D.C., M.T., A.G. and S.N.D.; resources, I.R.; data curation, M.T.; writing—original draft preparation, I.R.; writing—review and editing, I.R. and G.R.; supervision, I.R.; project administration, I.R. and G.R.; funding acquisition, I.R. and G.R. All authors have read and agreed to the published version of the manuscript.

Funding: This research received no external funding.

Data Availability Statement: All the relevant data are reported in the manuscript and in the Supplementary Materials.

Acknowledgments: The support of Fondazione Cariplo (Italy) in the form of research grants to Alice Gramegna and Simge Naz Degerli is gratefully acknowledged through the grant 2021-0855—"SCORE—Solar Energy for Circular CO_2 Photoconversion and Chemicals Regeneration", funded in the frame of the Circular Economy call 2021.

Conflicts of Interest: The authors declare no conflicts of interest.

References

1. Rossetti, I.; Tripodi, A. Catalytic Production of Renewable Hydrogen for Use in Fuel Cells: A Review Study. *Top. Catal.* **2022**. [CrossRef]
2. Gielen, D.; Boshell, F.; Saygin, D.; Bazilian, M.D.; Wagner, N.; Gorini, R. The role of renewable energy in the global energy transformation. *Energy Strateg. Rev.* **2019**, *24*, 38–50. [CrossRef]
3. Valera-Medina, A.; Amer-Hatem, F.; Azad, A.K.; Dedoussi, I.C.; De Joannon, M.; Fernandes, R.X.; Glarborg, P.; Hashemi, H.; He, X.; Mashruk, S.; et al. Review on ammonia as a potential fuel: From synthesis to economics. *Energy Fuels* **2021**, *35*, 6964–7029. [CrossRef]
4. Li, C.; Sage, V.; Wang, T.; Tang, L.; Yang, Y.; Lee, W.J.; Lippi, R.; Wang, F.; Kozielski, K.; Patel, J. Evaluation and outlook for Australian renewable energy export via circular liquid hydrogen carriers. *Int. J. Hydrogen Energy* **2023**, *49*, 1509–1527. [CrossRef]
5. Haydary, J.; Šuhaj, P.; Husár, J. Waste biomass to methanol–optimisation of gasification agent to feed ratio. *Biomass Convers. Biorrefin.* **2021**, *11*, 419–428. [CrossRef]
6. Kamarudin, S.K.; Shamsul, N.S.; Ghani, J.A.; Chia, S.K.; Liew, H.S.; Samsudin, A.S. Production of methanol from biomass waste via pyrolysis. *Bioresour. Technol.* **2013**, *129*, 463–468. [CrossRef]
7. Hussain, I.; Mustapha, U.; Al-Qathmi, A.T.; Malaibari, Z.O.; Alotaibi, S.; Samia; Alhooshani, K.; Ganiyu, S.A. The critical role of intrinsic physicochemical properties of catalysts for CO_2 hydrogenation to methanol: A state of the art review. *J. Ind. Eng. Chem.* **2023**, *128*, 95–126. [CrossRef]
8. Mierczynski, P.; Mosinska, M.; Maniukiewicz, W.; Nowosielska, M.; Czylkowska, A.; Szynkowska, M.I. Oxy-steam reforming of methanol on copper catalysts. *React. Kinet. Mech. Catal.* **2019**, *127*, 857–874. [CrossRef]
9. Compagnoni, M.; Tripodi, A.; Di Michele, A.; Sassi, P.; Signoretto, M.; Rossetti, I. Low Temperature Ethanol Steam Reforming: New Ni/MxO-ZrO_2 active and stable catalysts prepared by Flame Spray Pyrolysis. *Int. J. Hydrogen Energy* **2017**, *42*. *in press*. [CrossRef]
10. Madej-Lachowska, M.; Kulawska, M.; Słoczyński, J. Methanol as a high purity hydrogen source for fuel cells: A brief review of catalysts and rate expressions. *Chem. Process Eng.-Inz. Chem. i Proces.* **2017**, *38*, 147–162. [CrossRef]
11. Patel, S.; Pant, K.K. Kinetic modeling of oxidative steam reforming of methanol over $Cu/ZnO/CeO_2/Al_2O_3$ catalyst. *Appl. Catal. A Gen.* **2009**, *356*, 189–200. [CrossRef]
12. Mosińska, M.; Szynkowska-Jóźwik, M.I.; Mierczyński, P. Catalysts for hydrogen generation via oxy–steam reforming of methanol process. *Materials* **2020**, *13*, 5601. [CrossRef]
13. Kapran, A.Y.; Orlyk, S.M. Hydrogen Production in Methanol Reforming on Modified Copper–Zinc Catalysts: A Review. *Theor. Exp. Chem.* **2017**, *53*, 3–16. [CrossRef]
14. Glisenti, A.; Galenda, A.; Natile, M.M. Steam reforming and oxidative steam reforming of methanol and ethanol: The behaviour of $LaCo_{0.7}Cu_{0.3}O_3$. *Appl. Catal. A Gen.* **2013**, *453*, 102–112. [CrossRef]
15. Russo, D.; De Martino, M.; Di Benedetto, A.; Portarapillo, M.; Turco, M. Oxidative Methanol Reforming for Hydrogen-fed HT-PEMFC: Applications in the Naval Sector. *Chem. Eng. Trans.* **2023**, *99*, 367–372. [CrossRef]
16. Esposito, S.; Turco, M.; Bagnasco, G.; Cammarano, C.; Pernice, P.; Aronne, A. Highly dispersed sol-gel synthesized Cu-ZrO_2 materials as catalysts for oxidative steam reforming of methanol. *Appl. Catal. A Gen.* **2010**, *372*, 48–57. [CrossRef]
17. Pérez-Hernández, R.; Gutiérrez-Martínez, A.; Gutiérrez-Wing, C.E. Effect of Cu loading on CeO_2 for hydrogen production by oxidative steam reforming of methanol. *Int. J. Hydrogen Energy* **2007**, *32*, 2888–2894. [CrossRef]
18. Eaimsumang, S.; Petchakan, S.; Luengnaruemitchai, A. Dependence of the CeO_2 morphology in CuO/CeO_2 catalysts for the oxidative steam reforming of methanol. *React. Kinet. Mech. Catal.* **2019**, *127*, 669–690. [CrossRef]
19. Tesser, R.; Di Serio, M.; Santacesaria, E. Methanol steam reforming: A comparison of different kinetics in the simulation of a packed bed reactor. *Chem. Eng. J.* **2009**, *154*, 69–75. [CrossRef]
20. Nichele, V.; Signoretto, M.; Pinna, F.; Menegazzo, F.; Rossetti, I.; Cruciani, G.; Cerrato, G.; Di Michele, A. Ni/ZrO_2 catalysts in ethanol steam reforming: Inhibition of coke formation by CaO-doping. *Appl. Catal. B Environ.* **2014**, *150–151*, 12–20. [CrossRef]
21. Jeevanandam, P.; Pulimi, V.R.R. Synthesis of nanocrystalline NiO by sol-gel and homogeneous precipitation methods. *Indian J. Chem.—Sect. A Inorg. Phys. Theor. Anal. Chem.* **2012**, *51*, 586–590.
22. Giacomuzzi, R.A.M.; Portinari, M.; Rossetti, I.; Forni, L. A New Method for Preparing Nanometer-Size Perovskitic Catalysts for CH_4 Flameless Combustion. In *Studies in Surface Science and Catalysis*; Elsevier: Amsterdam, The Netherlands, 2000; Volume 130A.
23. Finocchio, E.; Rossetti, I.; Ramis, G. Redox properties of Co- and Cu-based catalysts for the steam reforming of ethanol. *Int. J. Hydrogen Energy* **2013**, *38*, 3213–3225. [CrossRef]
24. Chiarello, G.L.; Rossetti, I.; Forni, L.; Lopinto, P.; Migliavacca, G. Solvent nature effect in preparation of perovskites by flame-pyrolysis. 1. Carboxylic acids. *Appl. Catal. B Environ.* **2007**, *72*, 218–226. [CrossRef]

25. Chiarello, G.L.; Rossetti, I.; Forni, L.; Lopinto, P.; Migliavacca, G. Solvent nature effect in preparation of perovskites by flame pyrolysis. 2. Alcohols and alcohols + propionic acid mixtures. *Appl. Catal. B Environ.* **2007**, *72*, 227–232. [CrossRef]
26. Kydd, R.; Teoh, W.Y.; Wong, K.; Wang, Y.; Scott, J.; Zeng, Q.H.; Yu, A.B.; Zou, J.; Amal, R. Flame-synthesized ceria-supported copper dimers for preferential oxidation of CO. *Adv. Funct. Mater.* **2009**, *19*, 369–377. [CrossRef]
27. Compagnoni, M.; Lasso, J.; Di Michele, A.; Rossetti, I. Flame-pyrolysis-prepared catalysts for the steam reforming of ethanol. *Catal. Sci. Technol.* **2016**, *6*, 6247–6256. [CrossRef]
28. Chiarello, G.L.; Rossetti, I.; Lopinto, P.; Migliavacca, G.; Forni, L. Preparation by flame spray pyrolysis of ABO3 catalysts for the flameless combustion of methane. *Catal. Today* **2006**, *117*, 549–553. [CrossRef]
29. Cho, Y.-S.; Moon, J.W.; Chung, K.C.; Lee, J.-G. Synthesis of Nickel and Copper Nanopowders by Plasma Arc Evaporation. *J. Korean Powder Metall. Inst.* **2013**, *20*, 411–424. [CrossRef]
30. Roknabadi, R.; Mirzaei, A.A.; Atashi, H. Assessment of composition and calcination parameters in Fischer-Tropsch synthesis over Fe-Mn-Ce/γ -Al_2O_3 nanocatalyst. *Oil Gas Sci. Technol.* **2021**, *76*, 11. [CrossRef]
31. Deraz, N.M. The comparative jurisprudence of catalysts preparation methods: I. Precipitation and impregnation methods. *J. Ind. Environ. Chem.* **2018**, *2*, 19–21.
32. Rossetti, I.; Lasso, J.; Finocchio, E.; Ramis, G.; Nichele, V.; Signoretto, M.; Di Michele, A. TiO_2-supported catalysts for the steam reforming of ethanol. *Appl. Catal. A Gen.* **2014**, *477*, 42–53. [CrossRef]
33. *Advanced Selected Powder Diffraction Data, Miner. DBM*; J.C.P.D.S.: Swarthmore, PA, USA, 1974.
34. Scherrer, P.; Debye, P. Scherrer equation. *Physik* **1916**, *17*, 277–283.
35. Cychosz, K.A.; Thommes, M. Progress in the Physisorption Characterization of Nanoporous Gas Storage Materials. *Engineering* **2018**, *4*, 559–566. [CrossRef]
36. Zimmer, P.; Tschöpe, A.; Birringer, R. Temperature-programmed reaction spectroscopy of ceria- and Cu/ceria-supported oxide catalyst. *J. Catal.* **2002**, *205*, 339–345. [CrossRef]
37. Ratnasamy, P.; Srinivas, D.; Satyanarayana, C.V.V.; Manikandan, P.; Senthil Kumaran, R.S.; Sachin, M.; Shetti, V.N. Influence of the support on the preferential oxidation of CO in hydrogen-rich steam reformates over the CuO-CeO_2-ZrO_2 system. *J. Catal.* **2004**, *221*, 455–465. [CrossRef]
38. Luo, M.F.; Zhong, Y.J.; Yuan, X.X.; Zheng, X.M. TPR and TPD studies of CuO/CeO_2 catalysts for low temperature CO oxidation. *Appl. Catal. A Gen.* **1997**, *162*, 121–131. [CrossRef]
39. Avgouropoulos, G.; Ioannides, T. Effect of synthesis parameters on catalytic properties of CuO-CeO_2. *Appl. Catal. B Environ.* **2006**, *67*, 1–11. [CrossRef]
40. Yang, W.; Li, D.; Xu, D.; Wang, X. Effect of CeO_2 preparation method and Cu loading on CuO/CeO_2 catalysts for methane combustion. *J. Nat. Gas Chem.* **2009**, *18*, 458–466. [CrossRef]
41. Zou, H.; Dong, X.; Lin, W. Selective CO oxidation in hydrogen-rich gas over CuO/CeO_2 catalysts. *Appl. Surf. Sci.* **2006**, *253*, 2893–2898. [CrossRef]
42. Fierro, G.; Lo Jacono, M.; Inversi, M.; Porta, P.; Cioci, F.; Lavecchia, R. Study of the reducibility of copper in CuO-ZnO catalysts by temperature-programmed reduction. *Appl. Catal. A Gen.* **1996**, *137*, 327–348. [CrossRef]
43. Wang, W.; Li, X.; Zhang, Y.; Zhang, R.; Ge, H.; Bi, J.; Tang, M. Strong metal–support interactions between Ni and ZnO particles and their effect on the methanation performance of Ni/ZnO. *Catal. Sci. Technol.* **2017**, *7*, 4413–4421. [CrossRef]
44. Zedan, A.F.; AlJaber, A.S. Combustion synthesis of non-precious CuO-CeO_2 nanocrystalline catalysts with enhanced catalytic activity for methane oxidation. *Materials* **2019**, *12*, 878. [CrossRef]
45. Kundakovic, L.; Flytzani-Stephanopoulos, M. Cu- and Ag-modified cerium oxide catalysts for methane oxidation. *J. Catal.* **1998**, *179*, 203–221. [CrossRef]
46. Liu, W.; Flytzani-Stephanopoulos, M. Total oxidation of carbon monoxide and methane over transition metal fluorite oxide composite catalysts: I. Catalyst composition and activity. *J. Catal.* **1995**, *153*, 304–316. [CrossRef]
47. Udani, P.P.C.; Gunawardana, P.V.D.S.; Lee, H.C.; Kim, D.H. Steam reforming and oxidative steam reforming of methanol over CuO-CeO_2 catalysts. *Int. J. Hydrogen Energy* **2009**, *34*, 7648–7655. [CrossRef]
48. Li, M.; Amari, H.; van Veen, A.C. Metal-oxide interaction enhanced CO_2 activation in methanation over ceria supported nickel nanocrystallites. *Appl. Catal. B Environ.* **2018**, *239*, 27–35. [CrossRef]
49. Yang, S.-C.; Pang, S.H.; Sulmonetti, T.P.; Su, W.-N.; Lee, J.-F.; Hwang, B.-J.; Jones, C.W. Synergy between Ceria Oxygen Vacancies and Cu Nanoparticles Facilitates the Catalytic Conversion of CO_2 to CO under Mild Conditions. *ACS Catal.* **2018**, *8*, 12056–12066. [CrossRef]
50. Li, J.; Zhu, J.; Fu, S.; Tao, L.; Chu, B.; Qin, Q.; Wang, J.; Li, B.; Dong, L. Insight into copper-cerium catalysts with different Cu valence states for CO-SCR and in-situ DRIFTS study on reaction mechanism. *Fuel* **2023**, *339*, 126962. [CrossRef]
51. Chen, J.; Zhan, Y.; Zhu, J.; Chen, C.; Lin, X.; Zheng, Q. The synergetic mechanism between copper species and ceria in NO abatement over Cu/CeO_2 catalysts. *Appl. Catal. A Gen.* **2010**, *377*, 121–127. [CrossRef]
52. Liu, H.-X.; Li, S.-Q.; Wang, W.-W.; Yu, W.-Z.; Zhang, W.-J.; Ma, C.; Jia, C.-J. Partially sintered copper–ceria as excellent catalyst for the high-temperature reverse water gas shift reaction. *Nat. Commun.* **2022**, *13*, 867. [CrossRef]
53. Mierczynski, P.; Mierczynska, A.; Ciesielski, R.; Mosinska, M.; Nowosielska, M.; Czylkowska, A.; Maniukiewicz, W.; Szynkowska, M.I.; Vasilev, K. High active and selective Ni/CeO_2–Al_2O_3 and Pd–Ni/CeO_2–Al_2O_3 catalysts for oxy-steam reforming of methanol. *Catalysts* **2018**, *8*, 13–16. [CrossRef]

54. Pérez-Hernández, R.; Mondragón Galicia, G.; Mendoza Anaya, D.; Palacios, J.; Angeles-Chavez, C.; Arenas-Alatorre, J. Synthesis and characterization of bimetallic Cu-Ni/ZrO_2 nanocatalysts: H2 production by oxidative steam reforming of methanol. *Int. J. Hydrogen Energy* **2008**, *33*, 4569–4576. [CrossRef]
55. Mosinska, M.; Stępińska, N.; Maniukiewicz, W.; Rogowski, J.; Mierczynska-Vasilev, A.; Vasilev, K.; Szynkowska, M.I.; Mierczynski, P. Hydrogen production on Cu-Ni catalysts via the oxy-steam reforming of methanol. *Catalysts* **2020**, *10*, 273. [CrossRef]
56. Mierczynski, P.; Mosinska, M.; Zakrzewski, M.; Dawid, B.; Ciesielski, R.; Maniukiewicz, W.; Maniecki, T. Influence of the Zn–Al binary oxide composition on the physicochemical and catalytic properties of Ni catalysts in the oxy-steam reforming of methanol. *React. Kinet. Mech. Catal.* **2017**, *121*, 453–472. [CrossRef]
57. Mierczynski, P.; Vasilev, K.; Mierczynska, A.; Maniukiewicz, W.; Ciesielski, R.; Rogowski, J.; Szynkowska, I.M.; Trifonov, A.Y.; Dubkov, S.V.; Gromov, D.G.; et al. The effect of gold on modern bimetallic Au–Cu/MWCNT catalysts for the oxy-steam reforming of methanol. *Catal. Sci. Technol* **2016**, *6*, 4168–4183. [CrossRef]
58. Mierczynski, P.; Vasilev, K.; Mierczynska, A.; Maniukiewicz, W.; Szynkowska, M.I.; Maniecki, T.P. Bimetallic Au–Cu, Au–Ni catalysts supported onMWCNTs for oxy-steam reforming of methanol. *Appl. Catal. B Environ.* **2016**, *185*, 281–294. [CrossRef]
59. Luengnaruemitchai, A.; Pojanavaraphan, C.; Kumyam, A.; Thunyaratchatanon, C.; Gulari, E. Hydrogen production from the oxidative steam reforming of methanol over Au–Cu nanoparticles supported on Ce1-xZrxO_2 in a fixed-bed reactor. *Int. J. Hydrogen Energy* **2019**, *44*, 1686–1700. [CrossRef]
60. Rabe, S.; Vogel, F. A thermogravimetric study of the partial oxidation of methanol for hydrogen production over a Cu/ZnO/Al_2O_3 catalyst. *Appl. Catal. B Environ.* **2008**, *84*, 827–834. [CrossRef]
61. Yong, S.T.; Ooi, C.W.; Chai, S.P.; Wu, X.S. Review of methanol reforming-Cu-based catalysts, surface reaction mechanisms, and reaction schemes. *Int. J. Hydrogen Energy* **2013**, *38*, 9541–9552. [CrossRef]
62. Wachs, I.E.; Madix, R.J. The selective oxidation of CH_3OH to H_2CO on a copper(110) catalyst. *J. Catal.* **1978**, *53*, 208–227. [CrossRef]
63. Lee, J.K.; Ko, J.B.; Kim, D.H. Methanol steam reforming over Cu/ZnO/Al_2O_3 catalyst: Kinetics and effectiveness factor. *Appl. Catal. A Gen.* **2004**, *278*, 25–35. [CrossRef]
64. Sakong, S.; Gross, A. Total oxidation of methanol on Cu(110): A density functional theory study. *J. Phys. Chem. A* **2007**, *111*, 8814–8822. [CrossRef] [PubMed]
65. Manzoli, M.; Chiorino, A.; Boccuzzi, F. Decomposition and combined reforming of methanol to hydrogen: A FTIR and QMS study on Cu and Au catalysts supported on ZnO and TiO_2. *Appl. Catal. B Environ.* **2005**, *57*, 201–209. [CrossRef]
66. Yong, S.T.; Hidajat, K.; Kawi, S. The roles of Cu, Zn and Mn in $Cu_{0.5}Zn_{0.5}Mn_2O_4$ spinel-lattice catalyst for methanol decomposition. *Catal. Today* **2008**, *131*, 188–196. [CrossRef]